EPJ A
Hadrons and Nuclei

EPJ.org
your physics journal

Eur. Phys. J. A (2015) **51**: 185 DOI 10.1140/epja/i2015-15185-9

Perspectives for photonuclear research at the Extreme Light Infrastructure - Nuclear Physics (ELI-NP) facility

D. Filipescu et al.

Società Italiana di Fisica

Springer

Eur. Phys. J. A (2015) **51**: 185
DOI 10.1140/epja/i2015-15185-9

THE EUROPEAN PHYSICAL JOURNAL A

Review

Perspectives for photonuclear research at the Extreme Light Infrastructure - Nuclear Physics (ELI-NP) facility*

D. Filipescu[1,a], A. Anzalone[2], D.L. Balabanski[1], S.S. Belyshev[3], F. Camera[4,5], M. La Cognata[2], P. Constantin[1], L. Csige[6], P.V. Cuong[7], M. Cwiok[8], V. Derya[9], W. Dominik[8], M. Gai[10], S. Gales[1], I. Gheorghe[1,11], B.S. Ishkhanov[3,12], A. Krasznahorkay[6], A.A. Kuznetsov[12], C. Mazzocchi[8], V.N. Orlin[12], N. Pietralla[13], M. Sin[11], C. Spitaleri[2], K.A. Stopani[12], O. Tesileanu[1], C.A. Ur[1], I. Ursu[1], H. Utsunomiya[14,15], V.V. Varlamov[12], H.R. Weller[16,17], N.V. Zamfir[1], and A. Zilges[9]

[1] Extreme Light Infrastructure - Nuclear Physics (ELI-NP) / Horia Hulubei National Institute for R&D in Physics and Nuclear Engineering (IFIN-HH), Bucharest-Magurele, RO-077125, Romania
[2] INFN-LNS, via Santa Sofia 62, Catania, Italy
[3] Physics Faculty, Lomonosov Moscow State University, 119991 Moscow, Russia
[4] University of Milano, Departement of Physics, Via Celoria 16, Milano 1-20133, Italy
[5] INFN section of Milano Via Celoria 16, Milano 20133, Italy
[6] Institute of Nuclear Research, Hungarian Academy of Sciences (MTA Atomki), Post Office Box 51, H-4001 Debrecen, Hungary
[7] Centre of Nuclear Physics, Institute of Physics, Vietnam Academy of Science and Technology, Hanoi, Vietnam
[8] University of Warsaw, ul. Pasteura 5, 02-093 Warszawa, Poland
[9] Institute for Nuclear Physics, University of Cologne, Zülpicher Straße 77, D-50937 Cologne, Germany
[10] LNS at Avery Point, University of Connecticut, Groton, Connecticut 06340-6097, USA
[11] Nuclear Physics Department, University of Bucharest, Post Office Box MG-11, 077125 Bucharest-Magurele, Romania
[12] Skobeltsyn Institute of Nuclear Physics, Lomonosov Moscow State University, 119991 Moscow, Russia
[13] Institut fur Kernphysik, Technische Universitat Darmstadt, D-64289 Darmstadt, Germany
[14] Department of Physics, Konan University, Okamoto 8-9-1, Kobe 659-8501, Japan
[15] Center for Nuclear Study, University of Tokyo, 2-1 Hirosawa, Wako, Saitama 351-0198, Japan
[16] Triangle Universities Nuclear Laboratory, Durham, North Carolina 27708, USA
[17] Department of Physics, Duke University, Durham, North Carolina 27708, USA

Received: 6 May 2015 / Revised: 5 July 2015
Published online: 24 December 2015 –
Communicated by N. Alamanos

Abstract. The perspectives for photonuclear experiments at the new Extreme Light Infrastructure - Nuclear Physics (ELI-NP) facility are discussed in view of the need to accumulate novel and more precise nuclear data. The parameters of the ELI-NP gamma beam system are presented. The emerging experimental program, which will be realized at ELI-NP, is presented. Examples of day-one experiments with the nuclear resonance fluorescence technique, photonuclear reaction measurements, photofission experiments and studies of nuclear collective excitation modes and competition between various decay channels are discussed. The advantages which ELI-NP provides for all these experiments compared to the existing facilities are discussed.

1 Introduction 2
2 ELI-NP gamma beam system 3
2.1 Simulations of expected ELI-NP γ-ray beams . 4
3 Study of electromagnetic responses of atomic nuclei . 5
3.1 Nuclear resonance fluorescence 7
3.2 Gamma above neutron threshold experiments . 10
4 Photoneutron reaction cross-section measurements . 12
4.1 Present situation of photonuclear reaction data bases 12
4.2 Neutron multiplicity sorting measurements at ELI-NP 15
4.3 High-efficiency (γ, n) measurements for p-process nucleosynthesis 16
5 Charged particle emission in photoreactions 17
5.1 Nuclear structure 17
5.2 Gamma-charged particle reactions relevant to nuclear astrophysics 18

* Contribution to the Topical Issue "Perspectives on Nuclear Data for the Next Decade" edited by Nicolas Alamanos, Eric Bauge, Stéphane Hilaire.

[a] e-mail: dan.filipescu@eli-np.ro

6 Photofission studies 21
6.1 Previous results obtained by photofission 21
6.2 Excited states related to the fission barrier . . . 21
6.3 Theoretical predictions and experimental data available for the fission barrier 22
6.4 Rare fission modes, ternary fission 26
6.5 Detector developments 26
6.6 Simulations on photofission experiments 26
6.7 Separation and manipulation of neutron-rich isotopes 27
6.8 Summary on photofission experiments 27

1 Introduction

Some of the major questions which the international nuclear physics community addresses at present are: i) what new data will be obtained with new or upcoming experimental facilities, and ii) how could global collaboration be improved to enhance the quality of evaluated data. Here we introduce research opportunities and the experimental program which is under preparation at the Extreme Light Infrastructure - Nuclear Physics facility. ELI-NP is under construction in Magurele, Romania and is expected to become operational in 2018. It is a state-of-the-art laboratory dedicated to nuclear physics research with extreme electromagnetic fields and will host two 10 PW lasers and a very brilliant gamma-beam system. ELI-NP is designed to cross the frontiers of known physics and, in particular, thanks to the unique parameters of the gamma beam system, to allow precise photonuclear measurements in the energy region from 200 keV to 20 MeV. The experimental program of the facility was outlined in the ELI-NP White book [1] and presented in a number of papers [2,3].

Electromagnetic probes were among the first tools of investigating the atomic nucleus. The major problem of the photonuclear experiment is the type of photon source that is used. Most of the available data so far are obtained using bremsstrahlung photons. However, for precise measurements of, *e.g.*, photonuclear cross-sections, intense beams of monoenergetic photons are needed. ELI-NP will deliver intense very narrow bandwidth photon beams, which will be produced in inverse Compton backscattering of laser photons off a relativistic electron beam.

Several classes of experiments will be possible at ELI-NP, such as precise nuclear resonance fluorescence (NRF) experiments, direct measurements of photonuclear reaction cross-sections, photofission experiments and studies of nuclear collective excitation modes, as well as studies of the competition between various decay modes.

In NRF experiments photons are scattered off bound nuclear states. The method is proven to be an outstanding tool to investigate low-lying dipole excitations in atomic nuclei and to provide detailed spectroscopic information. For a recent review see [4]. These experiments will benefit from the ELI-NP high-flux, narrow bandwidth, nearly 100% polarized gamma beams and the availability of gamma-spectrometers of excellent energy resolution and high efficiency. The sensitivity and the spin-selectivity are essential for detailed studies of the fragmentation of the strength of specific collective dipole modes even at excitation energies where the total level density is high. In addition, the pencil beams at ELI-NP will allow the usage of small-size targets, which open opportunities for NRF research for nuclei which were not accessible so far, *e.g.* isotopes in the actinide region.

In the last decades accurate measurements revealed high importance of the pygmy dipole and M1-resonances built on top of the low-energy tail of giant dypole resonance (GDR). At ELI-NP, the 0.3% bandwidth of the polarized γ-ray beam will facilitate these studies and will provide an opportunity to investigate in detail the fragmentation of the strength of these excitations.

Reliable information on cross-sections of total and partial photoneutron reactions is extensively used in basic research to solve a number of fundamental problems of electromagnetic interactions. The traditional studies of the photonuclear reaction cross-sections in the region of the GDR explore roles of different types of nuclear excitations in photoabsorption and their coupling to collective nuclear degrees of freedom, competition of different final states and different mechanisms in the exit channels of the reactions and so on with the one of the ultimate goals to obtain good model description of observed cross-sections over the complete range of nuclei. Moreover, data on cross-sections for partial photoneutron reactions are widely used in various realms of science and technologies (nuclear physics and nuclear power engineering; radiation chemistry, geology, and medicine; materials science; ecology; monitoring luminosities of colliding beams of relativistic nuclei in accelerators and many other fields).

In recent years there is also a growing interest to measurements of near-threshold cross-sections of photoneutron reactions, which are required by many applications in astrophysics. These studies will benefit from the intense, narrow bandwidth γ-ray beams at ELI-NP. Since the radiative neutron capture cross-sections for short-lived radioactive nuclei are difficult to measure due to the fact that the measurements require both highly radioactive samples and intense neutron sources and assuming the Brink hypothesis, photodisintegration can be used to improve prediction of radiative neutron capture cross-sections by experimentally constraining the – strength function entering the statistical model calculations.

Photofission experiments at ELI-NP aim at studies of the fission-barrier landscape and investigation of rare fission modes. For a recent review see [5]. In addition, fission fragments produced in photofission, will be separated and manipulated in such way, that pure ion beams of radioactive isotopes will be produced and delivered to different measurement stations. This will provide a wealth of new experimental data on neutron-rich nuclei lying away of the β-stability valley.

2 ELI-NP gamma beam system

Until recently, fast positron in flight annihilation, tagged bremmstrahlung and radioisotopes produced by neutron or proton capture reactions represented the main sources

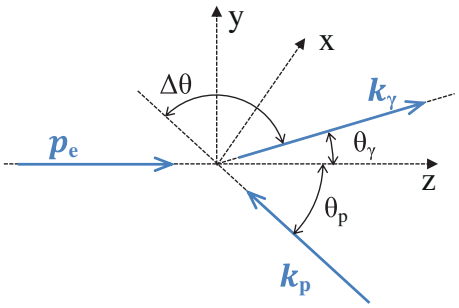

Fig. 1. Geometry of the inverse Compton scattering of a laser photon with $\hbar\boldsymbol{k}_\mathrm{p}$ momentum, incident at a polar angle θ_p with respect to the z-axis, and of a relativistic electron with momentum $\boldsymbol{p}_\mathrm{e}$, incident along the z-axis. The scattering takes place in the center of the coordinate system. The photon is scattered at an angle θ_γ with respect to the z-axis and with a momentum $\hbar\boldsymbol{k}_\gamma$. An in-plane scattering is represented. The angle between the direction of the incident and of the scattered photon is $\Delta\theta$.

for monochromatic γ-ray beams. During the last two decades, several facilities have been developed which provide quasi-monochromatic, pencil-like and highly polarized γ-ray beams using the inverse scattering of laser photons on relativistic electrons.

The geometry of the inverse Compton scattering between a laser photon of $\hbar\boldsymbol{k}_\mathrm{p}$ momentum, incident at a polar angle θ_p with respect to the z-axis, and a relativistic electron with momentum $\boldsymbol{p}_\mathrm{e}$, incident along the z axis is shown in fig. 1. The energy of the photon of $\hbar\boldsymbol{k}_\gamma$ momentum scattered at an angle θ_γ is given by

$$E_\gamma = \frac{(1+\beta\cos\theta_\mathrm{p})E_\mathrm{p}}{1-\beta\cos\theta_\gamma+(1-\cos\Delta\theta)E_\mathrm{p}/(\gamma\cdot m_0c^2)}\,, \qquad (1)$$

where E_p is the energy of the incident laser photon, m_0c^2 is the rest mass energy of an electron, $\beta = v/c$ is the speed of the incident electron relative to the speed of light, γ is the Lorentz factor for electron and $\Delta\theta$ is the angle between the momenta of the incident and scattered photons.

In collisions with relativistic electrons of several hundred megaelectronvolts, laser photons are scattered into a very narrow cone oriented closely to the direction of the incident electrons and their energy is amplified by a factor of 10^6–10^7, from eV to MeV energy range.

Because the energy of the scattered photons is strongly dependent on the scattering angle, collimators are used to produce quasi-monochromatic γ-ray beams. Up to a certain limit, the energy resolution of the laser Compton-scattered (LCS) γ-ray beam can be improved by decreasing the collimator opening. This limit is determined by the phase space distribution of the electron beam which is generally characterized in terms of the electron beam emittance. A small electron beam emittance lowers the limit on the collimator opening and increases the energy resolution of the γ-ray beam accordingly.

A currently operating γ-ray beam facility in Japan that employs conventional laser photons Compton-backscattered from relativistic electrons in a storage ring is the NewSUBARU synchrotron radiation facility [6]. At NewSUBARU, low-energy γ-ray beams at a few MeVs can be produced using a CO_2 laser ($\lambda = 10.59\,\mu$m) and high-energy γ-ray beams at a few tens of MeVs using a Nd:YVO_4 laser ($\lambda = 1.064\,\mu$m) in collisions with 0.5–1.5 GeV electrons. The highest γ-ray energy available at NewSUBARU is 76 MeV, which is achieved with use of a frequency-doubler module for the Nd:YVO_4 laser ($\lambda = 532$ nm). Real photon beams in the MeV region have been developed also at the National Institute of Advanced Industrial Science and Technology (AIST) in head on collisions of laser photons with electrons from the TERAS storage ring [7].

At the High-Intensity Gamma-Ray Source (HIγS) facility at Duke University [8], an electron beam is used to produce a Free Electron Laser beam in the eV range. Compton backscattering of this nearly 100% polarized beam from the several hundred MeV electrons in the storage ring leads to a photon beam in the MeV range.

At ELI-NP, γ-ray beams with energies between 0.2 to 19.5 MeV will be produced using a Yb:YAG laser ($\lambda = 515$ nm in the second harmonic) in collision with a high brightness electron beam provided by a warm linac. A comparison between the γ-ray beam energy range, energy resolution and intensity within bandwidth of NewSUBARU, HIγS and the ones expected at ELI-NP is made in table 1.

Up to $2.6\cdot10^5$ photons in FWHM bandwidth per one laser shot - electron beam interaction are expected to be provided by the ELI-NP gamma beam system. The 100 Hz laser pulses will be recirculated 32 times using a multi-pass recirculating system with a fixed focus point, constant crossing angle θ_p of 7.5° and shot to shot separation of 16 ns. A diagram of the ELI-NP gamma beam system time structure is displayed in fig. 2.

Table 1. Energy range, energy resolution and intensity within bandwidth values characteristic for the two existing facilities NewSUBARU [6,9] and HIγS [10] and the expected ones for ELI-NP [11].

	E_γ [MeV]	ΔE_γ [%]	I_γ^{bw} [ph/sec]
ELI-NP	0.2–19.5	< 0.5 (rms)	$8.3\cdot10^8$
NewSUBARU	0–76	> 1.2 (FWHM)	$\sim 10^5$
HIγS	0–100	0.8–10 (FWHM)	$\sim 10^7$

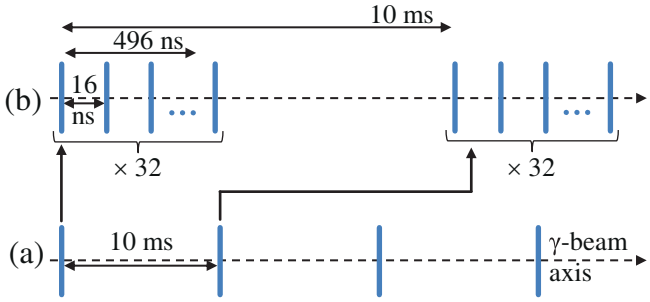

Fig. 2. Diagram of ELI-NP γ-ray beam time structure where (a) represents the 100 Hz macro-structure and (b) the γ-ray beam micro-structure. See text for details.

Table 2. Input parameters used for generating the spectra displayed in fig. 3: the electron beam emittance; $\sigma_{\rm ele}$ – electron beam transverse spot size at focal point; $E_{\rm ele}$ – electron beam energy; $\Delta E_{\rm ele}$ – electron beam relative energy resolution; $\lambda_{\rm laser}$ – laser beam wavelength; $\theta_{\rm p}$ – laser beam incident angle with respect to the electron beam axis; gamma-ray beam collimator opening; and the energy and energy resolution in FWHM of the simulated LCS γ-ray beams – E_γ and $\Delta E_\gamma^{\rm FWHM}$, respectively.

	Emittance [nm rad]	$\sigma_{\rm ele}$ [μm]	$E_{\rm ele}$ [MeV]	$\Delta E_{\rm ele}$ [%]	$\lambda_{\rm laser}$ [nm]	$\theta_{\rm p}$ [deg]	Collimator aperture	E_γ [MeV]	$\Delta E_\gamma^{\rm FWHM}$
ELI-NP	0.41	30	720	0.1	515	7.5	0.5 mm	18.55	0.5% 93 keV
NewSUBARU	x: 40 y: 4	x: 300 y: 180	1056.56	0.04	1064	0.	C1: 3 mm C2: 1 mm	$E_\gamma^{\rm max} = 18.68$ $E_\gamma^{\rm avg} = 17.79$	2.2% 411 keV

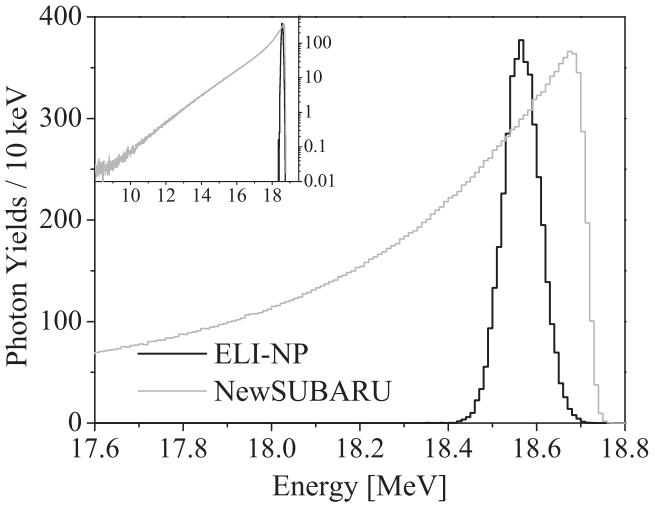

Fig. 3. Examples of simulated energy spectra for collimated LCS γ-ray beams incident on target typical for NewSUBARU and expected at ELI-NP. The input parameters and the energy and energy resolution for the two spectra are listed in table 2. The inset displays the two spectra on a wider energy range and shows the entire low-energy component typical for the NewSUBARU γ-ray beam.

2.1 Simulations of expected ELI-NP γ-ray beams

Figure 3 shows examples of energy spectra for collimated LCS γ-ray beams incident on target typical for NewSUBARU and expected at ELI-NP, where the latter is calculated in conformity with the electron and laser beam parameters published by the EuroGammaS consortium [11], the organization responsible for the development and delivery of the ELI-NP gamma beam system. The electron and laser beam energy, energy resolution and collision parameters used for generating the spectra displayed in fig. 3 are listed in table 2.

The spectra displayed in fig. 3 were obtained with a simulation code of the LCS γ-ray source developed using the Geant4 toolkit for the simulation of the passage of particles through matter [12,13]. A realistic model of laser photon - relativistic electron interaction was implemented in the code which takes into consideration the phase space distribution of the electron and laser beams. The simulation code was tested against experimental data taken at the LCS γ-ray beam facility NewSUBARU and it successfully reproduced both γ-ray energy and intensity profiles [9,14].

A 720 MeV electron beam energy with 0.1% relative energy resolution in collision with a 515 nm wavelength laser beam was considered for generating an example of an expected γ-ray beam spectrum on a target placed at 33 meters from the laser photons-electrons interaction point at ELI-NP. A 24 cm thick tungsten collimator with 0.5 mm diameter opening was employed for the ELI-NP scenario. For a γ-ray beam typical for NewSUBARU, a 1056.56 MeV electron beam energy with 0.04% relative energy resolution in collision with a 1064 nm wavelength laser beam were considered as input parameters. In this case, the γ-ray beam passes through two 10 cm thick lead collimators with 3 mm and 1 mm diameter openings, respectively, and the target is placed at 26 meters from the interaction point.

Although the ELI-NP electron beam is expected to have a 0.1% central energy resolution, higher than the 0.04% one at NewSUBARU, the electron beam emittance expected for ELI-NP is significantly lower than the one characteristic for NewSUBARU. Because of this, in the example given for ELI-NP, the energy spectrum of the scattered photons in a small angular spread $\Delta\theta_\gamma$ selected by collimation is a narrow —0.5% energy resolution in FWHM— and nearly simmetric distribution centered at the energy value $E_\gamma = 18.55$ MeV correponding to $\theta_\gamma = 0°$, $\theta_{\rm p} = 7.5°$ and given by eq. (1), where the collimator is placed along the electron beam axis. The typical γ-ray beam spectrum for NewSUBARU has a sharp high-energy front and a long low-energy tail. The maximum energy spectrum component at $E_\gamma^{\rm max} = 18.68$ MeV corresponds to photons backscattered in head-on collisions ($\theta_{\rm p} = 0°$ and $\theta_\gamma = 0°$) and its sharp front is given by the small electron beam energy resolution of 0.04%. The low-energy tail correponds to photons scattered at $\theta_\gamma \approx 0°$ from non head-on collisions with $\theta_{\rm p} > 0°$, which have a significant contribution to the total number of colisions given by the electron beam emittance value. The relative energy resolution of 2.2% in FWHM is obtained for this example. The low-energy tail shifts the average energy of the spectrum to $E_\gamma^{\rm avg} = 17.79$ MeV, approximately 1 MeV lower than the maximum energy.

Figure 4 shows the state and degree of polarization for a 19.5 MeV maximum energy uncollimated LCS γ-ray beam using the formalism of the Stokes parameters, where the first Stokes parameter represents the degree of linear polarization along the x-axis of a chartesian coordinate reference system having the z-axis along the electron

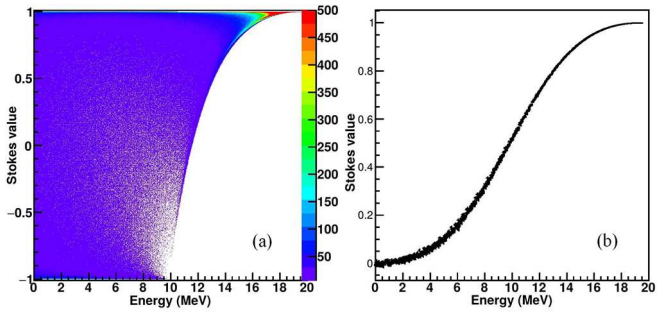

Fig. 4. Left: distribution of the first Stokes parameter for a LCS γ-ray beam with respect to the γ-ray energy. Right: the average of the same distribution for each energy bin. A 100% linearly polarized laser was employed.

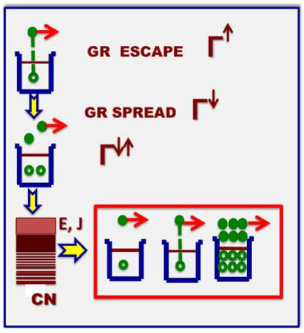

Fig. 5. Schematic view of the process of the direct decay and damping of giant resonances.

beam direction. The γ-ray beam is generated assuming a 100% linearly polarized laser beam with polarization angle $\tau = 90°$ incident at a $\theta_p = 7.5°$ with respect to the electron beam axis. As can be observed from the figure, the laser type and degree of polarization is conserved for the photons scattered in the direction along the electron beam axis, which corresponds to backscattering angles selected by collimation. The ELI-NP γ-ray beams are expected to be $> 99\%$ linearly polarized.

3 Study of electromagnetic responses of atomic nuclei

Photon-induced nuclear reactions mainly excite low-spin collective states like the isovector giant dipole resonance (IVGDR or simply GDR) which was discovered in 1937 [15] and characterized in 1947 [16] by sistematic studies on various nuclei. The IVGDR represents the strongest electric dipole response of nuclei originating from an out-of-phase dipole oscillation between protons and neutrons. In addition, the GDR mode can be excited not only when it is built on the ground state, but also when it is built on excited states (see, *e.g.*, [17,18]).

Such nuclear excited states decay by emission of particles or photons from the initial 1p-1h excitations or, due to internal mixing, are damped into a dense spectrum of more complex np-nh states toward a compound nucleus. The former process is characterized by the escape width $\Gamma^{\uparrow}$, while the damping is characterized by the spreading width $\Gamma^{\downarrow}$ (see fig. 5). The internal mixing occurs through a hierarchy of couplings towards more and more complex degrees of freedom. Collective motion is preferentially damped by 2p-2h components of the many-body wave function. The photon decay of GDR to the ground state and excited states provides information on the electromagnetic decay strength of GDR with multipole selectivity and the coupling of GDR to low-frequency collective modes.

The search for experimental evidence of scales associated with the coupling between collective states and internal and external degrees of freedom is a long-standing problem. Namely, the question whether or not the whole hierarchy of couplings (2p-2h, 3p-3h, etc.) manifests itself by giving evidence of finer structures in the line shape as the experimental resolution increases, is not fully solved. The fine structure measurement of the giant resonances decay may carry relevant information on the dominant damping mechanism and coupling scale. This can be achieved through the comparison between GDR excitation cross-section and the measurement of the GDR gamma decay direct to the ground state or low-lying states.

The pygmy dipole resonance (PDR) was discovered in the 21st century in the low-energy tail region of GDR as a new excitation mode related to the dipole oscillation of a neutron skin against a core nucleus [19,20] though there may be a different interpretation like low-energy E1 strength that fails to participate in the GDR excitation. The extra E1 strength exhausts a small fraction of the Thomas-Reiche-Kuhn (TRK) sum rule, typically below 1% for the stable $N = 82$ isotones [21], a few percent for ^{117}Sn [22], 7(3)% for ^{130}Sn, 4(3)% for ^{132}Sn [23] and 5(1.5)% for ^{68}Ni [24]. Besides the GDR, understanding the PDR is important to clarify the entire E1 response of nuclei.

M1 resonance of spin-flip nature ($\Delta l = 0$, $\Delta j = 1$) may emerge near neutron threshold in the tail of GDR typically in nuclei with the shell gaps starting from the magic number larger or equal to 28. Indeed, PDR and M1 resonances were reported in the nuclear resonance fluorescence [21,25–34], (p,p′) reactions [35–41], (γ, n) reactions [42,43], Coulomb dissociation [23] and the (^{3}He, ^{3}He′γ) reaction [22].

The Brink hypothesis [44] linking photo-deexcitation process to photoabsorption tells that the gamma-ray strength function of the low-energy tail of GDR governs the radiative neutron capture cross-section. Since they constitute extra strength of the low-energy tail of GDR, experimental information on the strength and resonance energy of PDR and M1 resonance is indispensable for a comprehensive understanding of the gamma-ray strength function. Indeed, it is shown that the PDR increases reaction rates of photodisintegration in the p-process nucleosynthesis [45] and radiative neutron capture on nuclei along the line of β-stability in the s-process nucleosynthesis [46]. The increase of the neutron capture rate occurs even more drastically on neutron-rich nuclei in the r-process nucleosynthesis [47–49].

We report here on various experimental methods employed to study the electric dipole response of atomic nuclei, focusing on real photon beams experiments. We treat separately experiments with γ-ray beams below and above neutron separation threshold, mainly because of the different characteristic detection systems.

Real photon beams based experiments provide reliable data on both excitation and decay modes of nuclear excited states. In this type of experiments, nuclei are irradiated with continuous or quasi-monochromatic γ-ray beams. For excitation energies below the particle separation threshold, (γ, γ') photon scatterings are induced and the nuclear resonance fluorescence method is employed for spectroscopy of γ decays. Photon beams with energies above the particle separation threshold induce mainly photo-dissociation reactions with emission of neutrons or charged particles. In this section we discuss angular and energy differential experiments of inelastic photon scattering and photo-neutron reactions. Absolute cross-sections, energies and angular distributions of decay products of photon scattering and photo-neutron reactions are the direct observables of such experiments. Because of the purely electromagnetic excitation mechanism, the energies, spins and parities of excited states, as well as decay branching ratios, multipole mixing ratios, decay widths and transition strengths can be extracted in a model independent way from them. Besides experiments using real photon beams, Coulomb excitation and hadronic excitation based experiments are also used for the investigation of nuclear collective modes.

Coulomb excitation experiments, such as inelastic proton scattering at intermediate energies at forward angles including 0° are an excellent tool for fine scanning of the photoabsorption cross-section in the GDR region. Recently, such experiments revealed PDR and M1 resonances in ^{208}Pb [41] and ^{90}Zr [40] and thus have drawn refreshed attention as a good probe of PDR and M1 resonance as well as GDR. Figure 6 shows E1 (upper panel) and M1 (lower panel) strength distributions in ^{90}Zr [40]. The dotted lines are the best-fit Lorentzian functions for PDR and M1 resonance. In the (p,p′) experiment, the E1 component is singled out as Coulomb excitation which dominates at very forward angles near 0°. In contrast, the determination of the M1 strength is rather indirect because it relies on the multipole-decomposition analysis of the proton angular distribution. Furthermore, the M1 excitation is induced strongly by nuclear interactions in the (p,p′) reaction. Therefore, the M1 strength observed in the (p,p′) reaction does not purely represent electromagnetic excitation strength. In this regard, γ-ray beams are obviously the best probe of investigating the electromagnetic property of nuclei. Also, although this type of experiment provides the excitation cross-section of the GDR, it gives no information on the GDR decay to ground or high-lying states through gamma or neutron emission.

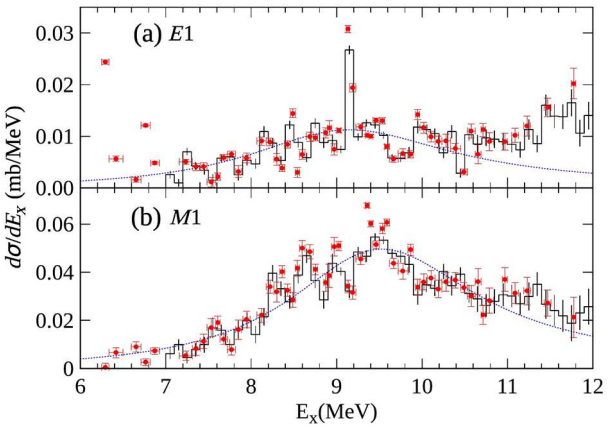

Fig. 6. E1 and M1 strength distributions in ^{90}Zr observed in (p,p′) reactions at 295 MeV. Reprinted figure with permission from ref. [40]. Copyright (2012) by the American Physical Society.

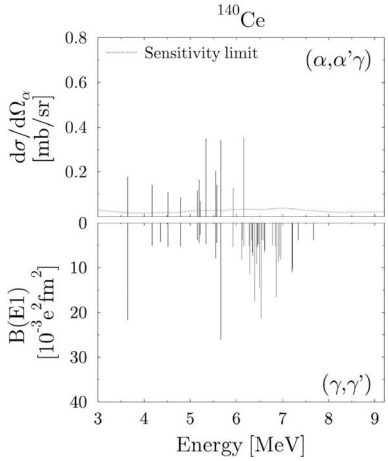

Fig. 7. Comparison of cross-sections measured in the $(\alpha, \alpha'\gamma)$ experiment (upper part) with B(E1) strengths derived from (γ, γ') (lower part) for ^{140}Ce. Reprinted figure from ref. [50] with permission from IOP publishing.

Hadronic interaction experiments at intermediate energies, such as inelastic alpha-particle scatterings, alongside experiments based on electromagnetic interaction, allow the investigation of the isoscalar and isovector nature of collective modes from the point of view of nuclear structure. Recent investigations by $(^{17}\mathrm{O}, ^{17}\mathrm{O}'\gamma)$ and $(\alpha, \alpha'\gamma)$ reactions in comparison with those by (γ, γ') reactions have shown that two E1 excitation modes are present in well-separated energy regions. Figure 7 shows a comparison of $(\alpha, \alpha'\gamma)$ cross-sections for ^{140}Ce [51] with B(E1) strengths derived from (γ, γ') reactions. One can see a strength over 3–6 MeV that is excited by both $(\alpha, \alpha'\gamma)$ and (γ, γ') reactions and a strength over 6–9 MeV that is excited only by (γ, γ') reactions. Similar results have been observed also when comparing the inelastic scattering of ^{17}O and (γ, γ') reactions [52–54].

According to the theoretical interpretation [55] based on the relativistic time blocking approximation [56] and quasi-particle phonon model [57], the low-energy strength

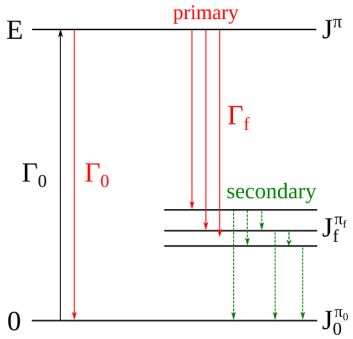

Fig. 8. Schematic picture of the NRF method. Excited states are populated by photons from the ground state and de-excite to the ground state either directly or via γ-ray cascades.

is consistent with the isospin mixed mode, while the high-energy strength with the isovector mode. Investigations by $(\alpha, \alpha'\gamma)$ and $(^{17}O, ^{17}O'\gamma)$ reactions are extended to ^{90}Zr, ^{138}Ba, ^{124}Sn ^{140}Ce, ^{208}Pb and ^{94}Mo, showing similar excitation patterns [20,52–54,50].

3.1 Nuclear resonance fluorescence

Nuclear resonance fluorescence or real-photon scattering is an ideal tool to obtain high-precision nuclear data below the particle threshold [59,4]. In NRF experiments the nucleus of interest is irradiated by an intense beam of photons with energies below the neutron and proton separation energies. Electromagnetic dipole (E1 and M1) and quadrupole (E2) transitions to bound states excited from the ground state are dominant. The subsequent γ decay of these excitations back to the ground state ("resonant de-excitation") and to excited energy levels of the nucleus (see fig. 8) can be observed with adequate photon detectors and allow the detailed analysis of the γ-ray transitions. Using HPGe semiconductor detectors for the γ-ray spectroscopy yields an excellent energy resolution in the range of a few keV, even at γ-ray energies close to the particle threshold. Scintillation detectors like $LaBr_3$ detectors have an inferior energy resolution to HPGe detectors, but deliver high detection efficiency and fast timing signals needed for certain applications. Due to the pure electromagnetic interaction for excitation and decay, NRF makes it possible to derive a large number of observables of a nucleus in a completely model-independent way which makes it an ideal tool for obtaining reliable nuclear data. These observables include:

– excitation energies (from ground-state decays), transition energies;
– spins of the excited states (from the measurement of angular correlations);
– parities of the excited states (in polarization sensitive experiments);
– decay branching ratios, decay widths;
– multipole mixing ratios (M1/E2 ratio);
– scattering cross-sections, absolute transition strengths.

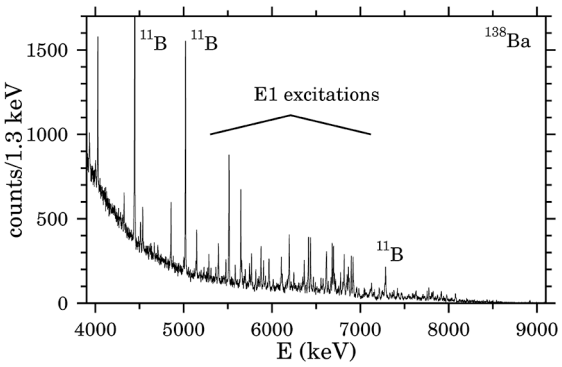

Fig. 9. Photon scattering spectrum of ^{138}Ba measured at the DHIPS facility at the S-DALINAC at TU Darmstadt. One can nicely identify isolated peaks mostly stemming from the E1 transition of $J^\pi = 1^-$ states to the ground state, ^{11}B calibration lines, and the strongly increasing continuous background at low energies. Reprinted from ref. [58], Copyright (2002), with permission from Elsevier.

There are two different types of γ-ray sources which are commonly used for the production of intense photon beams for NRF experiments: bremsstrahlung and laser Compton backscattering photon sources. The γ-ray beams delivered by these sources differ in basic beam properties, such as, the photon energy profile and polarization and, therefore, give access to the experimental observables mentioned above in slightly different ways. In the following we compare experiments using bremsstrahlung photons with experiments using photons from laser Compton backscattering facilities.

Bremsstrahlung photon beams generated by intense electron beams stopped in radiator targerts have been used to perform most NRF experiments in the past. This produces a continuous spectrum of photons up to the energy of the electron beam. Levels from the lowest energies up to this endpoint energy are excited in a single experiment simultaneously and their properties can be analyzed. One difficulty arises from a strongly increasing background from elastically scattered photons at lower energies which makes the observation of low-energy transitions to excited states challenging or even impossible. Figure 9 shows a typical γ-ray spectrum measured with a HPGe detector after irradiation of the target material with a bremsstrahlung beam. It was taken in a measurement on ^{138}Ba with an endpoint energy of 9.2 MeV [58]. Ground-state transitions from the various close-lying excited $J^\pi = 1^-$ states are clearly visible in the energy region between around 5 to 7 MeV and can be well separated with the excellent energy resolution of the HPGe detectors. Excitation energies, transition energies, spins, and cross-sections can be directly deduced from the observed ground-state transition strengths at 90° and 130° with respect to the beam axis.

In bremsstrahlung experiments, polarization observables can be obtained by using either the partly polarized off-axis part of the bremsstrahlung beam, or by us-

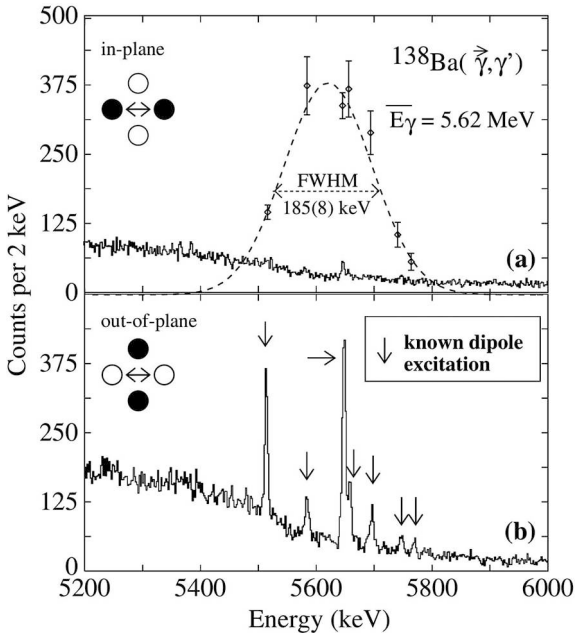

Fig. 10. The nearly 100% linearly polarized beams from laser Compton backscattering allow a straightforward parity determination by comparing decay spectra measured in- and out-of-plane with the polarization axis of the incoming photon beam. The dashed line in the upper panel indicates the beam-energy profile of the photon beam. Reprinted figure with permission from ref. [30]. Copyright (2002) by the American Physical Society.

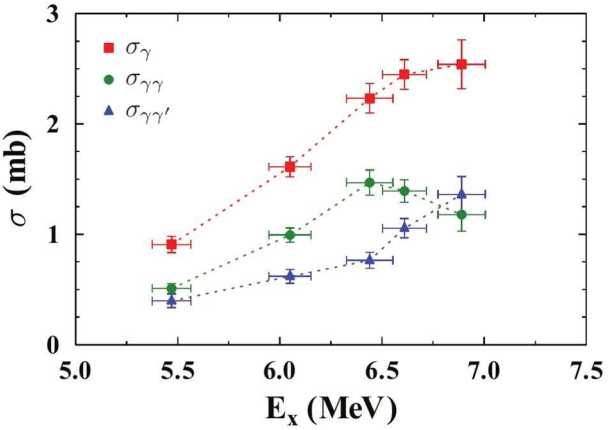

Fig. 11. The narrow bandwidth of the photon beam at HIγS allows a sensitive study of elastic ($\sigma_{\gamma\gamma}$), inelastic ($\sigma_{\gamma\gamma'}$), and total (σ_γ) photon-scattering cross-sections via the study of ground-state transitions, as well as secondary transitions of low-lying excited states. Reprinted figure with permission from ref. [60]. Copyright (2013) by the American Physical Society.

ing Compton polarimetry for the photons in the decay channel. Both methods are challenging and require usually time-consuming experiments, especially for excited states at higher energies. As a result, comprehensive parity studies are available from bremsstrahlung experiments for only a few selected isotopes. In the last decades, the dipole strength distribution of numerous isotopes has been studied systematically using the bremsstrahlung technique, mostly at the measuring sites of the electron accelerator at Gent University [61], the Stuttgart Dynamitron [59], the S-DALINAC (TU Darmstadt) [62], and the ELBE accelerator (FZ Dresden Rossendorf) [63]. A list of all isotopes studied in bremsstrahlung experiments has been published recently [64].

Laser Compton scattering γ-ray beams —nearly completely polarized and with quasi-monochromatic energy spectrum— allow to overcome many limitations of NRF experiments using bremsstrahlung. At energies relevant for nuclear structure studies, this technique was well exploited by experiments at the High-Intensity Gamma-Ray Source (HIγS) at Duke University [30]. At the TERAS storage ring an external laser has been used as the photon source [65], the same is true for the NewSUBARU storage ring [66]. Polarization is conserved during the Compton-scattering process which makes laser Compton backscattering an ideal tool for polarization physics (see fig. 10). Parity information for the known $J = 1$ states shown in fig. 10 is gained by a quantitative comparison of the ground-state transitions in the γ-ray spectra measured at $\theta = 90°$ in and out of the plane of the polarization axis of the incoming γ-ray beam. The experimental asymmetry of the photon intensities in the horizontal and vertical detectors is an ideal parity observable since the angular distribution of the de-exciting γ-rays strongly depends on the parity. The use of linearly polarized intense photon beams in NRF experiments allows for unambiguous and straightforward parity assignments, especially for dipole states in spin-zero nuclei.

The bandwidth ("monochromaticity") of the HIγS beam amounts to a few hundred keV which allows a selective excitation of states in a rather narrow energy window (see fig. 10(a)). The narrow beam energy profile has further advantage compared to continuous beam profiles. The selective excitation window increases the sensitivity to the determination of branching ratios via low-lying *primary* and *secondary* transitions *to* and *from* other excited states. These transitions have typically transition energies below the excitation window and can therefore be exclusively distinguished from elastic transitions decaying back to the ground state. Depending on the γ-ray spectroscopy setup single or $\gamma\gamma$ coincidence data can be acquired and used to deduce decay branchings. For coincidence measurements a higher coincidence efficiency can be achieved by using a combination of high-resolution HPGe detectors and high-efficiency $LaBr_3$ detectors as, *e.g.*, implemented for the high-efficiency $\gamma\gamma$ coincidence setup γ^3 at HIγS [68]. The determination of mean branching ratios from singles γ-ray spectra measured with HPGe detectors is possible by selecting the ground-state transitions of low-lying states which were prevously populated by the higher-lying states within the excitation-energy window. In this way, the inelastic part of the scattering cross-section is obtained in addition to the elastic scattering cross-section (see fig. 11).

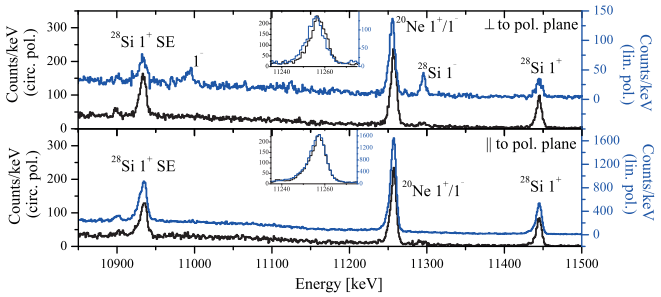

Fig. 12. Results of parity violation study using LCS γ-ray beams at HIγS. Summed spectra for the detectors placed perpendicular (top) and parallel (bottom) to the plane of polarization of the incident γ-ray beam. The spectra obtained with incoming linearly polarized beams (blue) use the right axis while the ones obtained with circularly polarized beams (black) use the left axis. The ^{20}Ne doublet states are represented in the insets. The energy difference between them is determined from the small energy shift between the linear and circular polarization in the detectors placed perpendicular to the polarization plane. The original figure is displayed in [67].

Experimental studies of parity doublets $J^{+/-}$ performed with almost completely polarized quasi-monochromatic γ-ray beams are a good method to observe the parity violation in nuclei. Usually, contributions of the weak interaction to the nuclear effective Hamiltonian are not well known, comparatively small, and neglected. Due to the parity-violating character of weak interaction, the physical doublet states contain an admixture of the opposite parity. Theory shows that this parity-violating admixture is enhanced if energy splitting of the double states has a comparable magnitude to the weak matrix element (typically of the order of 1 eV). In other words, good candidates are the parity doublets situated at very close energy to each other. One of the best candidates of such a study is the $1^+/1^-$ parity doublet in ^{20}Ne situated at ~ 11.25 MeV, which was recently investigated with Compton backscattering gamma rays at HIγS facility [67]. This experiment proved that the energy splitting of the doublet is $\sim 3.2(7)$ keV. One can imagine that using classical gamma spectroscopy methods is very difficult, if not impossible to disentangle the decays of the doublet to the ground state, not only because the corresponding gamma rays are very close in energy comparing to the capabilities of the best gamma spectrometers that exist nowadays, but also the intensity of the two lines differs by a factor of 45 (I(M1) $\gg$ I(E1)). For this reason, in the previous experiments, not only that the energy splitting was measured with poorer precision (7.7 ± 5.5 keV), but also the order of the levels was different.

Using the correlation between the polarization plane of the incident gamma beam and the azimuthal emission angle of electric and magnetic radiations, it was possible to measure the energy splitting and gamma ray intensities with higher precision. Figure 12 shows how the centroid of ~ 11.25 MeV transitions shifts from the spectra acquired with HPGe detectors placed in the plane of polarization to the spectra acquired with HPGe detectors placed perpendicular to the plane of polarization. In this experiment, the only limitations in achieving a higher analyzing power are the real size of the irradiated target and the distance between target and detectors. In other words, a higher-intensity and better focused gamma beam compared to the one from HIγS would be beneficial for this type of experiments. Also a higher energy resolution would allow a smoother levels scan. Thus, the superior characteristics of the ELI-NP γ-ray beam promise a higher degree of precision for this technique of parity violation studies.

The ELI-NP photon beam will be produced via Compton backscattering of an external laser beam on relativistic electrons. The unique property of the ELI-NP photon beam from the gamma beam system with respect to NRF measurements is the concentration of the photon flux in a very narrow bandwidth which allows the effective and selective population of single nuclear states. In addition the very small beam diameter allows the high-precision study of rare or even radioactive isotopes because NRF experiments with target masses of a few mg become feasible (compared to several 100 mg of target material which are needed at existing facilities). Furthermore, an increase in beam intensity of more than a factor of 10 as compared to what is presently available at the HIγS facility is anticipated. One limitation of ELI-NP arises from the anticipated time structure of the beam. The macropulse rate of 100 Hz will make it necessary to use segmented HPGe Clover detectors in order to avoid serious pile-up problems in the spectra. Nevertheless, ELI-NP will not only make it possible to study physics beyond the existing frontiers, but it will also become an important source of new nuclear data. This will include systematic and comprehensive studies of the parities of bound $J = 1$ states, high-precision determinations of the decay patterns of exited states and cross-sections for the dipole and quadrupole excitations in rare and radioactive isotopes.

3.2 Gamma above neutron threshold experiments

Experiments above the neutron separation threshold (S_n) will be performed alongside NRF studies for a complete investigation of the nuclear photon absorption process and its decay modes. Energy and angular differential photoneutron reactions and elastic and inelastic (γ, γ') scatterings are discussed in this section, while photon-induced charged particles emission and integral photo-neutron experiments will be discussed in the following sections.

Figure 13 depicts the complex branchings of neutron and gamma decay of excited states above neutron threshold. Excited states above the S_n of nucleus ^{A}X undergo with highest probability neutron decays to the ground state and excited states in the residual nucleus $^{A-1}$X. The neutron decays to excited states below the neutron emission threshold in $^{A-1}$X followed by γ cascades towards the ground state belong to the $(\gamma, 1n)$ channel. The neutron decay is in competition with the significantly less

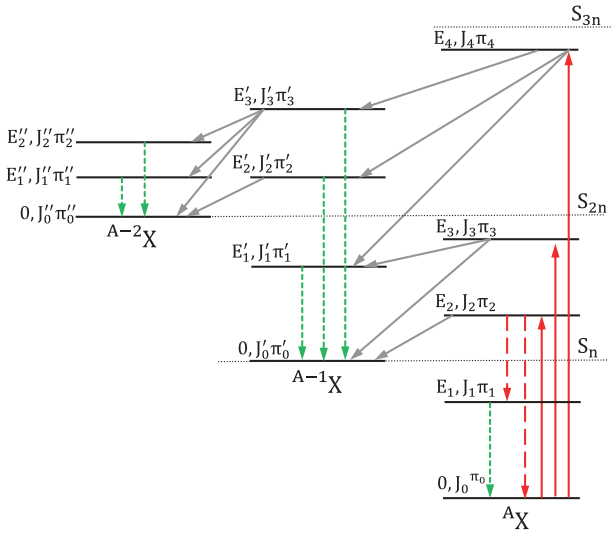

Fig. 13. Schematic view of complex neutron decays of giant resonances.

probable γ-ray decay mode to the ground state or to excited states in ^{A}X. Photoexcitations above S_{2n} can lead also to neutron decays to excited states above the neutron emission threshold in the residual nucleus $^{A-1}$X, which in turn decay by neutron emission to excited states or to the ground state of the residual nucleus $^{A-2}$X in the $(\gamma, 2n)$ channel. The observation of the energy and angular distibution of neutron and gamma decays of the photon excited giant resonance states in stable and unstable nuclei provide valuable nuclear data such as:

- energy of excited states, neutron decays and γ-ray transitions;
- neutron/gamma decay branching ratios;
- (γ, xn), (γ, γ) and (γ, γ') excitation cross-sections, absolute transition strengths;
- multipolarity of reaction neutrons, multipole mixing ratios of γ transitions;
- spin and parity of excited states.

For bremsstrahlung photon beams based experiments, which represent the majority of the photonuclear experiments, the energy of the nuclear states excited by photons is determined by spectroscopic measurements of decay products, as the energy spectrum of the incident beam is continuous. While in the case of NRF measurements high energy resolution detectors as HPGe are available for the analysis of γ transitions, for photoneutron reactions the neutron measurements generally lack the energy resolution needed for identifyng the populated nuclear state.

Therefore, experimental data of E1 and M1 resonances above S_n are very scarce, especially for high excitation energies, where neutron decays to both excited states and the ground state of the residual nucleus are possible and therefore the energy of the emitted neutron does not uniquely determine the energy of the photon which induced the reaction. Individual states starting from the neutron threshold up to $\sim$ 1 MeV excited using bremsstrahlung photon beams were resolved by time-of-flight

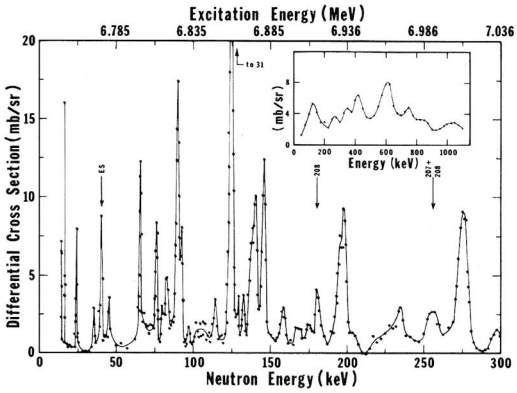

Fig. 14. Differential ^{207}Pb(γ, n) cross-section measured at 135° using the neutron threshold technique using bremsstrahlung beam of 8.4 MeV end-point energy. Contaminating peaks from ^{208}Pb and transitions to excited states in ^{206}Pb are indicated by arrows. The (γ, n) cross-section averaged with a 40 keV square smoothing function is shown in the inset. Reprinted figure with permission from ref. [69]. Copyright (1971) by the American Physical Society.

spectroscopy of slow and intermediate energy neutrons in nuclei such as ^{206,207,208}Pb, ^{56,57}Fe, ^{52,53}Cr, ^{24,25,26}Mg, ^{19}F [70] using the neutron threshold method described in [71]. Figure 14 shows 135° diferential photoneutron cross-sections for ^{207}Pb obtained with the threshold neutron technique [69], where one can see prominent peak structure with E1 and M1 nature. Spin assignments were determined in such experiments by measuring the differential (γ, n) cross-section for the nucleus of study at two different angles, 90° and 135°, as in the case of ^{208}Pb described in [70,42]. This technique is limited to a narrow excitation energy range between the neutron threshold and the first excited state in a residual nucleus, where only neutron decay to the ground state in a residual nucleus is detected.

Laser Compton scattering γ-ray beams selectively excite the nuclear states in a narrow energy window given by the energy resolution of the LCS γ-ray beam and are more suitable than continuous spectrum beams for the investigation of the competition between various decay modes of E1 and M1 resonances above neutron emission threshold. In LCS γ-ray beam experiments, information on the excitation energy is given both by the incident quasi-monochromatic photon beam and by spectroscopy of reaction products.

Recently, partial photoneutron reaction cross-sections on ^{207}Pb and ^{208}Pb have been measured at the AIST facility using LCS γ-ray beams of 4.6%–16.8% energy resolution in FWHM and $\sim$ 93% degree of polarization [72]. An attempt was made of separating E1 and M1 photoexcitations above neutron threshold in ^{207}Pb and ^{208}Pb by measuring anisotropies of neutron emission to separate s- and p-wave neutrons with slow neutron detectors of long-counter type. Although this measurement has successfully identified the total strength of PDR above neutron threshold, it lacked great energy resolution.

Energy and angular distributions of neutron and γ decays of nuclear states excited by the γ-ray beam are proposed to be recorded at ELI-NP with a high energy resolution, high detection efficiency array of appropriate neutron and photon detectors covering large energy and angular ranges.

Scintillation detectors such as $LaBr_3$ or $CeBr_3$ ones are proposed to be used for detection of γ-rays emitted following neutron decays or in (γ,γ) and (γ,γ') reactions. Such detectors allow to distinguish the full-energy peak of $> 10\,\mathrm{MeV}$ γ-rays from the first escape peak and provide fast response highly necessary because of the 16 ns repetition structure of the ELI-NP γ-ray beam. High energy resolution HPGe detectors may be used for fine selections of γ-rays emitted following neutron decays.

Neutron energies are determined with the time-of flight technique and neutron angular distributions are measured to identify E1 and M1 resonances. The Li glass scintillator is suited to detection of low-energy neutrons because of the large reaction Q-value (4.78 MeV) of the $^6\mathrm{Li}(\mathrm{n},\alpha)^3\mathrm{H}$ reaction, while the liquid scintillation detector with relatively low light output against recoil protons in the n + p scattering is suited to detection of high-energy neutrons.

A multi-detector array consisting of 34 3×3 inch $LaBr_3$ or $CeBr_3$ detectors placed at 25 cm from the irradiated target and 62 20×5 cm BC501 liquid scintillator and ^{6}Li neutron detectors placed at 1.5 m from the target is envisioned at ELI-NP.

Neutron decay branching ratios of excited states of GDR to different states in the residual nuclei will be investigated in detail for the first time using the combination between the highly monochromatic γ-ray beam and the complex detection system proposed at ELI-NP.

The maximum energy of the ELI-NP γ-ray beam of 19.5 MeV is well above the centroid of the GDR and below the three neutron emission threshold in most nuclei. As shown in fig. 13, excited states below the S_{3n} of the ^{A}X nucleus can decay either by $(\gamma,1\mathrm{n})$ channel with emission of neutrons to excited or ground state of $^{A-1}$X or by $(\gamma,2\mathrm{n})$ channel with succesive neutron emissions to excited or ground state of $^{A-1}$X and $^{A-2}$X nuclei. Minute experimental data of such exclusive decays of GDR provide invaluable information on nuclear structure of GDR.

The energy of the excited states in nuclei irradiated with the best monochromatic γ-ray beam of ELI-NP will be precisely known with 0.3% energy resolution in 1σ and the energy of neutrons will be known within $\sim 10\%$ using the TOF method. However, it is not possible to pin down individual exclusive decays of GDR in heavy nuclei solely by neutron detection because of the limited energy resolution and dense level schemes of residual nuclei. Thus, to unambiguously identify all the branchings in the neutron decay of GDR, neutron (n) - gamma (γ) or n-γ-γ coincidences with neutron and γ-ray detectors are required.

Elastic and inelastic photon scattering at excitation energies above the particle emission threshold is strongly supressed by the particle decay channel. Experimental data on (γ,γ) and (γ,γ') reactions above S_n are extremely scarce because of their very low cross-sections and the difficulty of precisely determining the excitation and decay energy. The unique intensity, energy resolution and polarization parameters of the ELI-NP γ-ray beam will allow for the first time the measurement of the excitation function and the branching ratio of the decay to the ground state and to low-lying excited states in the energy region around and above the particle binding energy.

The electric or magnetic type of the emitted radiation can be experimentally extracted because of the polarization of the ELI-NP beam and this provides, in very detail, the nature of the dipole excitation. In even-even nuclei, the reaction mechanism is purely electromagnetic and we can easily assume that the main excited states are dipole states because of the 0^+ ground state. As the ground state decay should scale as $\mathrm{E}^3\times\mathrm{B(E1)}$, the experiment provides a measurement of the energy dependence of the B(E1). The measurement of both $\sigma(\gamma,\gamma)$ (which is sensitive to the B(E1)), and $\sigma(\gamma,\mathrm{n})$ (which is sensitive to the wave function) is an important and challenging point for the theory.

An experimental campaign focused on the measurement of gamma decay of GDR and PDR states decay to the ground state and to excited states in ^{208}Pb is proposed as a first day experiment at ELI-NP. The dipole response of ^{208}Pb was widely studied theoretically and the excitation photo-absorption cross-section was recently measured by [41], therefore the GDR excitation cross-section measured at ELI-NP will be cross-checked for validation with precise data existing in literature. Only few data on gamma decay (for E^* > particle binding energy) with large uncertainties on the excitation energy are available and will be used as a calibration [73]. These data provide a ground-state photon branching ratio in the energy interval 9.5–25 MeV of 0.019 ± 0.002.

E1 and M1 photoexcitations above the neutron emission threshold will be identified and separated by measuring angular distributions of neutron emission with the detection array described above. Special emphasis is placed on odd-N nuclei with neutron thresholds as low as 6 MeV. Nearly full strengths of PDR and spin-flip M1 resonance are expected to emerge above neutron threshold for odd-N nuclei. The present investigation of PDR and M1 resonance with emphasis on odd-N nuclei above neutron threshold is complementary to the investigation with the NRF technique with emphasis on even-even nuclei below neutron threshold.

The excitation energy of interest is expected not to exceed the two-neutron separation energy (S_{2n}). When photoexcitation does not exceed the first excited state in a residual nucleus ($E_\gamma < S_n + E_x^{1^{st}}$), neutron decay of PDR and M1 resonance takes place to the ground state as in the case of the threshold neutron experiment. However, when it exceeds, neutron decays to excited states can take place in competition with the ground-state decay.

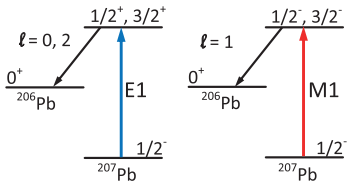

Fig. 15. Excitation and neutron decays of PDR and M1 resonance in ^{207}Pb.

Figure 15 depicts E1 and M1 photoexcitations of ^{207}Pb. The selection rule of spin and parity tells that the E1 excitation of the ^{207}Pb in the ground state ($1/2^-$) to the $1/2^+$ and $3/2^+$ states is followed by s- and d-wave neutron decay to the ground state ^{206}Pb, while the M1 excitation into $1/2^-$ and $3/2^-$ states is by p-wave neutron decay. In the photoexcitation near neutron threshold, the d-wave neutron emission is strongly suppressed by the centrifugal potential compared to the s-wave neutron emission. One can find the same correlation of E1 (M1) photoexcitation with the s-wave (p-wave) neutron emission for ^{208}Pb.

Obviously s-wave neutrons are emitted isotropically. In contrast, when the photoexcitation is induced by linearly polarized γ-rays, the p-wave neutron emission is characterized by the angular distribution,

$$W_p(\theta, \Phi) = \frac{3}{8\pi}[\sin^2\theta \cdot (1 + \cos 2\Phi)], \qquad (2)$$

where θ is the polar angle with respect to the z-axis chosen along incident direction of the γ-ray beam and Φ is the azimuthal angle with respect to the x-axis chosen along the electric field (linear polarization).

4 Photoneutron reaction cross-section measurements

The main problem of a photonuclear experiment is the type of the photon source that can be used to obtain intense beams of monoenergetic photons. Different methods of effectively generating quasi-monoenergetic photon energy spectrum were used to measure photonuclear cross-sections. Most of the available cross-sections were obtained using bremsstrahlung (BR) [74] and quasi-monoenergetic annihilation (QMA) photons [75,76] produced by positron annihilation in flight.

4.1 Present situation of photonuclear reaction data bases

The BR spectrum is continuous. Therefore, the reaction yield $Y(E_m)$ which is measured experimentally corresponds to the cross-section folded with the spectrum

$$Y(E_{\rm m}) = \int_{E_{\rm th}}^{E_{\rm m}} W(E_{\rm m}, E)\sigma(E){\rm d}E, \qquad (3)$$

where $\sigma(E)$ is the reaction cross-section and $W(E_{\rm m}, E)$ is the BR-spectrum with end-point energy $E_{\rm m}$.

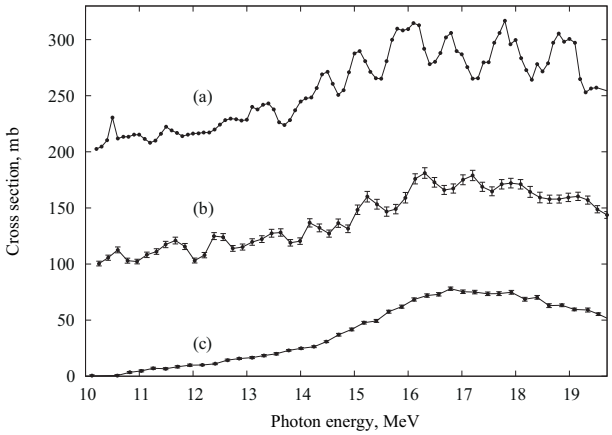

Fig. 16. ^{63}Cu$(\gamma, 1n)^{62}$Cu reaction cross-sections (a) obtained in the BR- experiment [80] ($\Delta E = 210$ keV); (b) obtained by re-processing of the QMA yield difference $Y_{e+} - Y_{e-}$ [81] with $\Delta E = 210$ keV and (c) the published [81] cross-sections corresponding to the QMA yield difference $Y_{e+} - Y_{e-} \approx \sigma(E)$ with $\Delta E \sim 200$–400 keV.

The cross-section $\sigma(E)$ can be obtained from the yield Y using standard mathematical methods to solve the inverse problem [77]. If the BR end-point energies used in a series of measurements of the reaction yield are close enough, the reaction cross-section can be obtained as if the effective photon spectrum takes a form of a quasimonoenergetic (close to Gaussian) line.

Real QMA spectra produced by annihilation of positrons in flight [75,76] allows to avoid the unfolding procedure and measure the cross-section directly. The majority of measurements with the QMA photons were performed at Lawrence Livermore National Laboratory (USA) and Centre d'Etudes Nucleaires de Saclay (France). However, since the QMA photons are mixed with the BR generated by positrons, three steps are needed to filter out the unwanted contribution: 1) measurements of the reaction yield $Y_{e+}(E_{\rm m}, E)$ with the QMA photons which are accompanied by the BR; 2) measurements of the reaction yield $Y_{e-}(E_{\rm m}, E)$ with the BR produced by electrons at the same energy; 3) after normalization and subtraction of the latter yield from the former one, the resulting quantity $Y(E_{\rm m}, E) = Y_{e+}(E_{\rm m}, E) - Y_{e-}(E_{\rm m}, E)$ is interpreted as a measured reaction cross-section. The QMA-photon intensity is typically low, and the resultant cross-sections suffer from two flaws: the accuracy of the normalization is often poor and the energy resolution is of the order of several hundred keV at best.

Compared to the BR-based experiments, the QMA-based experiments reveal noticeably less structure in the reaction cross-section for the majority of nuclei exception several nuclei with $A < 30$. The effective line width of the QMA-photons is broadened due to the presence of a prominent BR continuum produced by positrons. It is possible to refine the energy resolution by performing some additional processing (unfolding) [78]. An example of such re-processing of the experimental ^{63}Cu$(\gamma, 1n)^{62}$Cu reaction yields [77] using the method of reduction [79] is shown in fig. 16 in comparison with the original data and the re-

sult of the BR experiment [80] for the energy range up to the $(\gamma, 2n)$ reaction threshold $B_{2n} = 19.7\,\mathrm{MeV}$.

One can see that the structure of the cross-section unfolded from the results of the QMA photon experiment is very close to that obtained in the BR experiment. Similar results were obtained after reprocessing [82] of the photoneutron yield reaction cross-sections,

$$\sigma(\gamma, Sn) = \sigma(\gamma, 1n) + 2\sigma(\gamma, 2n) + 3\sigma(\gamma, 3n) + \ldots, \quad (4)$$

for ^{16}O [83,84] and ^{197}Au [85]. Therefore, it is concluded that the QMA cross-sections are strongly over-smoothed (real energy resolution is 3–4 times less than previously believed) in comparison with the characteristic width of the intermediate structure of the GDR. Due to the effective resolution of the QMA technique being significantly lower than expected ($\sim$ 1.3–1.6 MeV), fine structures (such as the PD and M1 resonances) visible in the cross-sections obtained in BR experiments are not observed when using QMA. It would be very helpful if new intense monoenergetic γ-beams, that will become available at the ELI-NP facility, could be used to re-measure some of the single-neutron reaction cross-sections.

The effective photon line shapes are very different in the QMA- and BR-based experiments, which also leads to apparent systematic discrepancies in both amplitudes (absolute value) and shapes (intermediate structure) of the cross-section. A detailed comparison [80] of the ^{18}O$(\gamma, 1n)$ cross-sections obtained using BR photons [86] and QMA photons [82] showed that the resonances have larger amplitudes and smaller widths in BR as compared to the QMA photon cross-sections: the amplitude ratio $A_{\mathrm{BR}}/A_{\mathrm{QMA}}$ varies from 1.00 to 1.28, while the width ratio $w_{\mathrm{QMA}}/w_{\mathrm{BR}}$ varies from 1.00 to 2.25.

Partial photoneutron cross-sections obtained with the QMA photons at Livermore and Saclay suffer from systematic discrepancies ($\sim$ 100%) [87,88]: in many cases, the $(\gamma, 1n)$ reaction cross-sections are noticeably larger at Saclay than at Livermore, whereas the $(\gamma, 2n)$ cross-sections in turn are larger at Livermore than at Saclay.

The systematics of integrated cross-section ratios (Saclay/Livermore) $R = \sigma_{\mathrm{S}}/\sigma_{\mathrm{L}}$ calculated in [87,88] for 19 nuclei (^{51}V, ^{75}As, ^{89}Y, ^{90}Zr, ^{115}In, ^{116,117,118,120,124}Sn, ^{127}I, ^{133}Cs, ^{159}Tb, ^{165}Ho, ^{181}Ta, ^{197}Au, ^{208}Pb, ^{232}Th, ^{238}U) is shown in fig. 17. One can see large discrepancies in the ratios for the 1n and 2n channels. The average ratio is $\sim$ 1.08 in the 1n channel, while it is 0.82 in the 2n channel, as shown by the dotted lines in the figure.

It has been suggested [89,90] that the discrepancy in the partial reaction cross-sections originated from the procedure of neutron multiplicity sorting. Additionally using the activation technique, it was shown that the Saclay data of $\sigma(\gamma, 2n)$ is significantly underestimated (and correspondingly $\sigma(\gamma, 1n)$ overestimated) because of large systematic uncertainties.

In order to further examine the discrepancy, a new approach has been developed for evaluating partial photoneutron cross-sections [91,92].

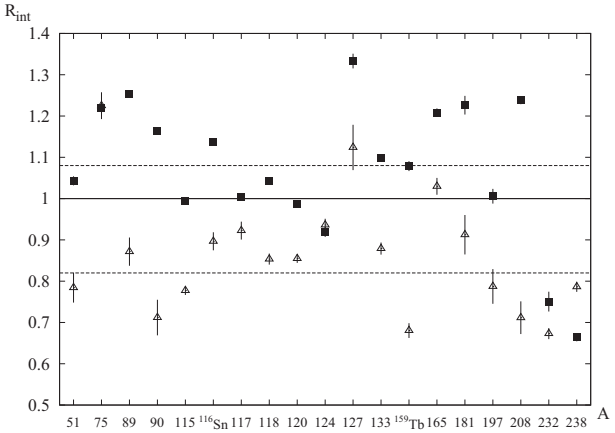

Fig. 17. Systematics of integrated cross-section ratios (Saclay/Livermore) $R = \sigma_{\mathrm{S}}/\sigma_{\mathrm{L}}$ for 1n (squares) and 2n (triangles).

The objective criteria for analyzing systematic uncertainties are proposed based on the ratios of partial photoneutron reaction cross-sections to the photoneutron yield cross-section

$$\begin{aligned} \mathrm{F}_x &= \sigma(\gamma, x\,n)/\sigma(\gamma, \mathrm{Sn}) \\ &= \sigma(\gamma, x\,n)/[\sigma(\gamma, 1n) + 2\sigma(\gamma, 2n) + 3\sigma(\gamma, 3n) + \ldots]. \end{aligned} \quad (5)$$

According to the definition given by eq. (5), F_1 is the ratio of $\sigma(\gamma, 1n)$ to the sum $[\sigma(\gamma, 1n)+2\sigma(\gamma, 2n)+3\sigma(\gamma, 3n)+\ldots]$ and, therefore, can never be greater than 1.00; correspondingly F_2 can never be greater than 0.50 and so on. If the experimental F_x value is larger than the corresponding upper limit, $1/x$, it is an unambiguous indication of unreliable neutron multiplicity assignment.

Several studies [87,91–96] of experimental data for ^{90,91,94}Zr, ^{115}In, ^{112,114,116,117,118,119,120,122,124}Sn, ^{159}Tb, ^{181}Ta, ^{188,189,190,192}Os, ^{197}Au and ^{208}Pb show that, as a rule, the partial reaction cross-sections do not satisfy the proposed criteria of reliability. The effect is the most evident in the case of ^{116}Sn and ^{159}Tb [93]. The corresponding experimental data in comparison with the results of theoretical calculations [97,98] are shown in figs. 18 and 19.

One can see that both the ^{116}Sn$(\gamma, 1n)$ reaction cross-section in the energy range of 21–26 MeV and the ^{156}Tb$(\gamma, 1n)$ reaction cross-section in the range of 18–22 MeV take negative values which are correlated with values $\mathrm{F}_2^{\mathrm{exp}} > 0.5$. This is an indication of incorrect sorting of neutrons into multiplicity 1 and 2. For ^{116}Sn the sharp fall of $\mathrm{F}_2^{\mathrm{exp}}$ at energies $E > 26\,\mathrm{MeV}$ (just below the 3n threshold B_{3n}) means that additionally sorting of neutrons into multiplicity 2 and 3 is incorrect. For ^{156}Tb at the energy $E > 25\,\mathrm{MeV}$ $\mathrm{F}_2^{\mathrm{exp}}$ have the values near 2.0 (it means that $\sigma(\gamma, 2n)$ is twice as large as $\sigma(\gamma, \mathrm{Sn})$!). It again indicates that sorting of neutrons into multiplicity 2 and 3 is definitely incorrect.

A new method of evaluating partial photoneutron reaction cross-sections was proposed to examine the unrelia-

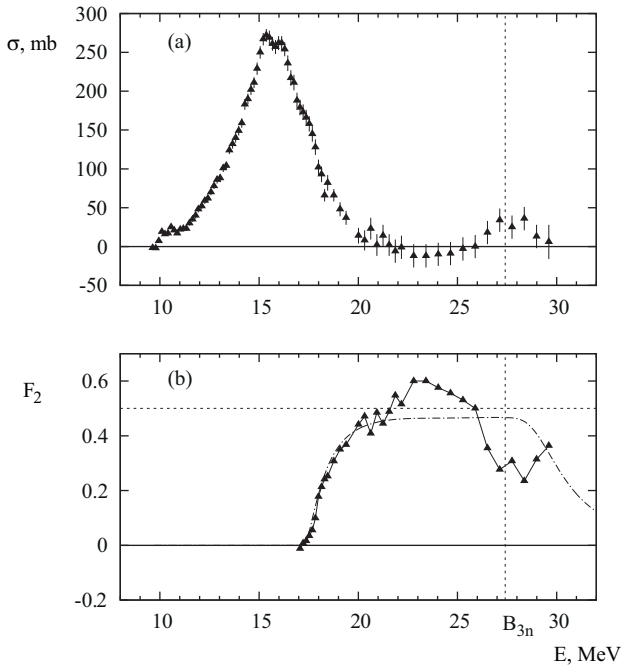

Fig. 18. Comparison of experimental $(\gamma, 1n)$ reaction cross-sections (a) and functions F_2^{exp} (triangles) and F_2^{theor} ([97,98] dot-dashed line) (b) for ^{116}Sn [99].

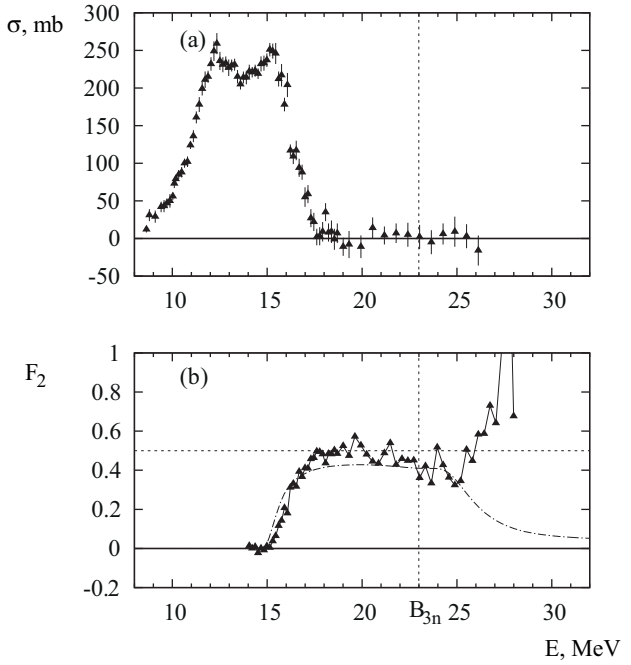

Fig. 19. Same as fig. 18 but for ^{156}Tb [84].

bility of the available experimental data sets. The method is based on the neutron yield cross-section $\sigma_{\rm exp}(\gamma, {\rm Sn})$ (eq. (4)) that is not affected by neutron multiplicity and the combined model of photonuclear reactions [97,98] which is used to calculate theoretical functions $F_x^{\rm theor}$ and decompose the neutron yield cross-section into the partial reaction cross-sections:

$$\sigma_{\rm eval}(\gamma, xn) = F_i^{\rm theor}\sigma_{\rm exp}(\gamma, {\rm Sn}) = [\sigma_{\rm theor}(\gamma, xn)/\sigma_{\rm theor}(\gamma, {\rm Sn})]\sigma_{\rm exp}(\gamma, {\rm Sn}). \quad (6)$$

Numerous comparisons [87,91–96] show that the evaluated cross-sections often significantly disagree with the results of the neutron multiplicity sorting experiments, but agree with the results of activation experiments. Independent measurements of the $(\gamma, 1n)$ and $(\gamma, 2n)$ reaction cross-sections using the highly monoenergetic γ-beam at ELI-NP are indeed of great importance to resolve the discrepancy issue.

Laser Compton scattering γ-ray beams are an ideal tool for direct measurements of photoneutron reaction cross-sections because of their quasi-monochromatic spectra obtained by collimation, as described in sect. 2. During the last decade, using laser Compton backscattered γ-ray beams and a detection system based on the moderation of reaction neutrons, photoneutron cross-sections have been measured for 13 elements (D, Be, Se, Mo, Zr, Pd, Sn, La, Pr, W, Re, Os, Ta, Au, Pb) and 38 isotopes at AIST [7], and for 4 elements (Ge, Nd, Sm, Dy) and 15 isotopes at the NewSUBARU synchrotron radiation facility. The measurements were however limited to $(\gamma, {\rm n})$ cross-sections near neutron threshold.

A high-efficiency 4π neutron detector developed at the Konan University is currently in use at the NewSUBARU [9]. The reaction neutrons emitted from the irradiated target with energies up to $\sim 1\,$MeV in the $(\gamma, {\rm n})$ cross-section measurement, are moderated in a polyethylene block and recorded by 20 ^{3}He neutron counters placed in three concentric rings around the beam axis. The neutron detection efficiency varies from approximately 75% for thermal neutrons down to $\sim 60\%$ for 1 MeV neutrons.

Because no information on the energy of the neutrons can be obtained from the detector's signal, the so-called ring ratio technique developed by Berman and Fultz [75] is employed for determining the average energy of the neutron spectra. As the volume of moderating material between the neutron source and each ring of counters is different, the ratio of the numbers of neutrons detected in two different rings of ^{3}He proportional counters depends on the neutron energy. As the three ring ratios in a different way depend on the original neutron energy, they can be used to determine the average neutron energy.

Figure 20 represents experimental cross-sections for the ^{142,144}Nd$(\gamma, {\rm n})$ reactions. The ^{142}Nd$(\gamma, {\rm n})$ reaction was investigated independently using QMA γ-ray beams at the Saclay facility [100], BR γ-ray beams [103] and LCS γ-ray beams produced at the AIST facility [101]. Cross-sections for the ^{144}Nd$(\gamma, {\rm n})$ reaction were measured using QMA γ-ray beams at the Saclay facility [100] and LCS γ-ray beams produced at NewSUBARU [102].

While a good agreement is observed between the BR data and the LCS measurements performed at AIST for the ^{142}Nd$(\gamma, {\rm n})$ reaction, the QMA data are sistematically higher than the LCS and BR ones by a $\sim$ 1.18 factor

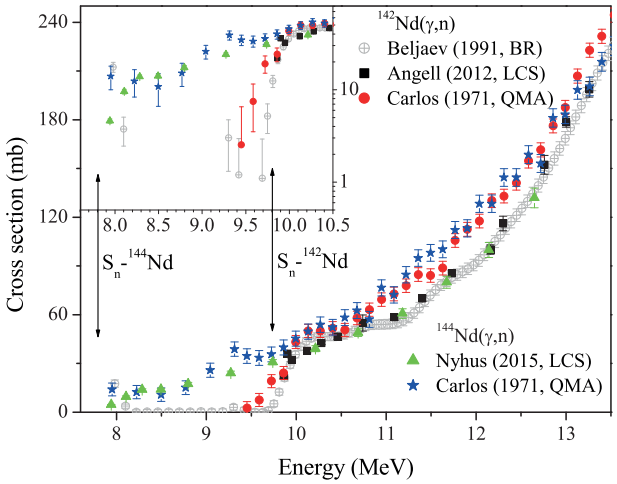

Fig. 20. Experimental photoneutron reaction cross-sections for ^{142,144}Nd measured with QMA [100], LCS [101,102] and BR [103] beams. The energy region in the close vicinity of the neutron emission threshold values for the two isotopes is magnified and represented in the inset for better visualization.

for both reactions. As can be observed in the inset from fig. 20, the LCS γ-ray beams with energy resolutions as low as 1.2% provided at the NewSUBARU facility enable accurate cross-section measurements much closer to the neutron emission threshold compared to the $\sim 8\%$ energy resolution γ-ray beams provided at the AIST facility.

4.2 Neutron multiplicity sorting measurements at ELI-NP

Because the discrepancies between the Livermore and Saclay data cannot be resolved in any systematic way [78, 92], there is a growing interest in an improvement of the IAEA-TECDOC-1178 [104] based on such research activities as acquisition and evaluation of new data. Experimental efforts will be dedicated at ELI-NP to partial and total photoneutron cross-section measurements for the GDR. The maximum γ-ray energy is 19 MeV at ELI-NP so that the maximum neutron multiplicity is limited to 2. A novel technique of sorting the neutron multiplicity is required to address the serious discrepancy in $(\gamma, 1n)$ and $(\gamma, 2n)$ cross sections between the Livermore and Saclay data [78,92]. We present here details of the neutron multiplicity sorting technique with a flat-efficiency neutron detector.

Let us consider (γ, xn) cross-section measurements with a 4π neutron detector similar to the one developed at the Konan University, described in sect. 4.1. We limit our discussion to (γ, xn) cross-section measurements with $x = 1$ and 2 at ELI-NP with the intense and monochromatic γ-ray beam whose maximum energy is 19 MeV. The number of single neutron (1n) and double neutron (2n) events experimentally observed, N_s and N_d, are respectively expressed by

$$N_s = N_1 \cdot \varepsilon(E_1) + N_2 \cdot {}_2C_1 \cdot \varepsilon(E_2)(1 - \varepsilon(E_2)) \quad (7)$$

and

$$N_d = N_2 \cdot \varepsilon(E_2)^2, \quad (8)$$

where N_1 and N_2 are the number of neutrons emitted from the $(\gamma, 1n)$ and $(\gamma, 2n)$ reactions, respectively, and ε is the total neutron detection efficiency of the 4π neutron detector. Obviously, the N_1 and N_2 are proportional to the reaction cross-sections, $\sigma(\gamma, 1n)$ and $\sigma(\gamma, 2n)$.

The ring-ratio technique can be applied to the double neutron event (N_d) to deduce the average neutron energy, E_2. However, the average neutron energy E_1 for the $(\gamma, 1n)$ channel cannot be determined by applying the technique to the single neutron event (N_s) because N_s consists of two contributions from the $(\gamma, 1n)$ and $(\gamma, 2n)$ reactions (see eq. (7)). Namely, the detection efficiency cannot be determined separately for the $(\gamma, 1n)$ and $(\gamma, 2n)$ reaction channels. This is a fatal defect associated with the ring-ratio technique in the neutron multiplicity sorting with a 4π neutron detector whose detection efficiency strongly depends on neutron energy.

To overcome the defect of the ring-ratio technique in neutron multiplicity sorting, it is essential to develop a flat efficiency 4π neutron detector whose detection efficiency is independent of neutron energy. Using Monte Carlos simulations with the Geant4 code, the neutron detection system used at NewSUBARU was modified in search of a configuration which ensures a flat efficiency. The flatness was achieved by compensating the strong energy dependence of the efficiency of the inner ring, which rapidly decreases with increasing neutron energy, by those of the middle and outer ring, which increases with increasing energy. For this, the total number of detectors was increased to 30 keeping the number of counters on the inner ring constant and each of the three rings was placed further away from the beam axis. A total efficiency of 40–37.5% over a neutron energy range 0–4 MeV and 40–35% over 0–5 MeV was obtained.

4.3 High-efficiency (γ, n) measurements for p-process nucleosynthesis

The majority of nuclides heavier than iron are synthesized by the slow (s) and rapid (r) neutron captures with nearly equal ($\sim 50\%$) shares of nucleosynthesis, which proceed along the line of β-stability and in the neutron-rich region of the chart of nuclei, respectively. On top of them, there are thirty-five nuclei referred to as the p-nuclei produced by the reprocessing of pre-existing seed nuclei of the s- and r-type by a combination of (p, γ) captures and (γ, n), (γ, p) or (γ, α) photoreactions complemented by β^+ decay, electron captures, and (n, γ) reactions. As a natural result of the re-processing, the p-process nuclides are neutron-deficient and rare in natural abundance (0.01 to 1%, exceptionally of the order of 10% in the $A \sim 90$ region, as listed in table 3).

Photodisintegrations play the leading role in the p-process, whereas the (p, γ) reactions appear to contribute only and probably marginally, to the production of the lightest p-nuclei. Temperatures larger than about $T_9 = 1.5$

Table 3. List of the 35 isotopes classified as *p*-nuclei, with their solar system abundances relative to 10^6 Si atoms proposed by the Anders and Grevesse compilation [105]. There are no experimental data on photon induced reactions on the nuclei marked with * in the fourth column.

Nucleus	Natural abundance [%]	Abundance (10^6 Si) [105]	
^{74}Se	0.89	0.55	
^{78}Kr	0.35	0.153	*
^{84}Sr	0.56	0.132	
^{92}Mo	14.84	0.378	
^{94}Mo	9.25	0.236	
^{96}Ru	5.54	0.103	
^{98}Ru	1.87	0.035	
^{102}Pd	1.02	0.0142	
^{106}Cd	1.25	0.0201	
^{108}Cd	0.89	0.0143	
^{113}In	4.29	0.0079	
^{112}Sn	0.97	0.0372	
^{114}Sn	0.66	0.0252	
^{115}Sn	0.34	0.0129	*
^{120}Te	0.09	0.0043	
^{124}Xe	0.09	0.00571	
^{126}Xe	0.09	0.00509	*
^{130}Ba	0.106	0.00476	
^{132}Ba	0.101	0.00453	
^{138}La	0.09	0.000409	*
^{136}Ce	0.185	0.00216	*
^{138}Ce	0.251	0.00284	
^{144}Sm	3.07	0.008	
^{152}Gd	0.2	0.00066	
^{156}Dy	0.06	0.000221	
^{158}Dy	0.1	0.000378	*
^{162}Er	0.14	0.000351	*
^{164}Er	1.61	0.00404	*
^{168}Yb	0.13	0.000322	
^{174}Hf	0.16	0.000249	*
^{180}Ta	0.012	2.48E-06	*
^{180}W	0.12	0.000173	
^{184}Os	0.02	0.000122	*
^{190}Pt	0.014	0.00017	
^{196}Hg	0.15	0.00048	

($T_9 = T/10^9$ K, where T is the temperature in Kelvin) are required for photodisintegrations to take place on time scales comparable to stellar evolutional ones, and may not exceed $T_9 = 3.5$ in order to avoid the photoerosion of all the heavy nuclei to more stable nuclei in the "iron peak". It is also necessary to freeze-out the photodisintegrations on a short enough time scale, typically of the order of one second. Those constraints are nicely met in the deep O-Ne layers of massive stars exploding as type II supernovae (SNa-II). The SNe-II is undoubtedly the most studied and the most successful scenario for the *p*-process [106–108]. Other plausible sites for the *p*-process, like presupernova burning phases of massive stars or the explosion of type-Ia supernovae, have been explored [109].

The significance of photonuclear reactions has revived in the context of the *p*-process nucleosynthesis, which was triggered and has been enhanced by the emergence of the laser Compton-scattering (LCS) γ-ray beam [110]. Photoneutron cross-sections can be measured with the LCS γ-ray beams at existing facilities like HIGS [8] and NewSUBARU [6] using ~ 1 g isotopic targets. Since the natural abundance of the *p*-nuclides is small, $\sigma(\gamma, \mathrm{n})$ measurements relevant for the *p*-process require γ-ray beams with intensity higher by three orders of magnitude than that available at the existing facilities, provided that typically 1 mg samples of *p*-nuclides are available commercially. Among the 35 *p*-nuclei, especially two odd-odd *p*-nuclides, ^{180}Ta and ^{138}La await an experimental challenge to measurements of the $^{180}\mathrm{Ta}(\gamma, \mathrm{n})^{179}\mathrm{Ta}$ and $^{138}\mathrm{La}(\gamma, \mathrm{n})^{137}\mathrm{La}$ reactions [109, 110].

The odd-odd nuclide ^{180}Ta has the remarkable property of having a short-lived ($T_{1/2} = 8.15$ h) $J^\pi = 1^+$ ground state ($^{180}\mathrm{Ta}^g$) and a very long-lived ($T_{1/2} > 1.2 \times 10^{15}$ yr) $J^\pi = 9^-$ isomeric state ($^{180}\mathrm{Ta}^m$). Its minute abundance ($^{180}\mathrm{Ta}^m/^{181}\mathrm{Ta} \approx 10^{-4}$) gives $^{180}\mathrm{Ta}^m$ the status of the only naturally occurring isomer and the rarest element in nature. The $^{180}\mathrm{Ta}^m$ yield predictions are affected by uncertainties concerning the $^{181}\mathrm{Ta}(\gamma, \mathrm{n})^{180}\mathrm{Ta}$ and $^{180}\mathrm{Ta}(\gamma, \mathrm{n})^{179}\mathrm{Ta}$ photodisintegrations rates which most directly influence the $^{180}\mathrm{Ta}^m$ production and destruction.

The $^{181}\mathrm{Ta}(\gamma, \mathrm{n})^{180}\mathrm{Ta}$ reaction has been measured directly by [45], the relative production by this reaction of the ground and isomeric states of ^{180}Ta being obtained experimentally as well by [111, 112]. The $^{180}\mathrm{Ta}^m(\mathrm{n}, \gamma)^{181}\mathrm{Ta}$ cross-section has been measured by [113]. This experimental information can enter the calculation of the rate of the reverse photodisintegration of direct interest through the application of the reciprocity theorem. It is however noted that the total $^{181}\mathrm{Ta}(\gamma, \mathrm{n})^{180}\mathrm{Ta}$ cross-section suffices to determine the production rate of $^{180}\mathrm{Ta}^m$ under the condition of thermalization between the ground state and the isomeric state in ^{180}Ta which is considered to hold in the deep O-Ne layers of exploding massive stars (SNa-II).

The $^{180}\mathrm{Ta}(\gamma, \mathrm{n})^{179}\mathrm{Ta}$ cross-section cannot be estimated from experimental data using the reciprocity theorem, the radiative neutron capture cross-section on the unstable ^{179}Ta being unmeasured. Therefore, the measurement of the rate of $^{180}\mathrm{Ta}(\gamma, \mathrm{n})^{179}\mathrm{Ta}$ is a highly necessary complement to the already measured one on ^{181}Ta in order to correctly predict the $^{180}\mathrm{Ta}^m$ yield.

In spite of its very small abundance ($^{138}\mathrm{La}/^{139}\mathrm{La} \approx 10^{-3}$), the odd-odd neutron deficient heavy nuclide ^{138}La is underproduced in all *p*-process calculations performed so far. This results from an unfavorable balance between its main production by $^{139}\mathrm{La}(\gamma, \mathrm{n})^{138}\mathrm{La}$ and its main destruction by $^{138}\mathrm{La}(\gamma, \mathrm{n})^{137}\mathrm{La}$, even in the *p*-process layers which are the most favorable to the ^{138}La production. These zones are the O-Ne layers of the considered mas-

sive stars explosively heated to peak temperatures around $T_9 = 2.4$. While the (γ, n) cross-section has been measured for ^{139}La [114], that for ^{138}La has long been out of experimental reach. It is also noted that the two measurements of the β^- spectra of ^{138}La suffer from a significant disagreement with the standard theory [115,116].

The nuclear reaction input adopted for the *p*-process calculations concerning the ^{138,139}La photodisintegration rates of direct relevance to the question of the production of ^{138}La is represented by the reverse (n, γ) reaction rates. Using these values, the (γ, n) rates are evaluated by the application of the reciprocity theorem. A direct measurement of the photodisintegration of ^{138}La would be highly valuable for the *p*-process calculations concerning the nucleosynthesis of ^{138}La. Due to the scarcity of ^{138}La, the high-intensity gamma beam provided by ELI-NP is the perfect tool to induce measurable (γ, n) on this isotope.

5 Charged particle emission in photoreactions

A Silicon Strip Detector (SSD) and electronic readout TPC (eTPC) are proposed for measuring charged particles emanating from the interactions of high-energy gamma-rays of the ELI-NP. These studies will provide several research opportunities in nuclear structure physics and nuclear astrophysics. We discuss below a few examples of such research projects. We do not present a complete list of experiments that we envisage with charged particle detectors at the ELI-NP facility, but we rather expand on some of the highlights of our proposed research projects.

5.1 Nuclear structure

The structure of light nuclei, and specifically of clustering received new impetus due to major developments of *ab initio* calculations of light nuclei and in particular of ^{12}C. Theoretical *ab initio* shell model [117] and symmetry inspired shell model [118] calculations as well as *ab initio* Effective Field Theory (EFT) calculations on the lattice [119,120], Fermionic Molecular Dynamics (FMD) model [121] and Antisymmetrized Molecular Dynamics (AMD) model [122], are employed to yield a microscopic foundation for the clustering phenomena that naturally occurs in cluster models [123,124]. For example, one issue of current concern [125] is the structure of the three alpha-particles in the Hoyle state at 7.65 MeV in ^{12}C (*e.g.*, linear chain, obtuse triangle or equilateral triangle) and the Hoyle rotational band built on top of the Hoyle state [126–130].

A recent experiment performed at the HIγS gamma-ray facility [131] using an optical readout TPC (O-TPC) [132] indeed provided unambiguous identification of the 2^+ member of the Hoyle rotational band. As an example of Nuclear Structure studies that we propose to perform at the ELI-NP with our proposed e-TPC and SSD detectors, we consider measurements of the multi-alpha decay of ^{12}C and ^{16}O with a TPC detector. Such measurements of multi-alpha decay of ^{12}C were also performed in the past with SSD [133–135] hence similar measurements

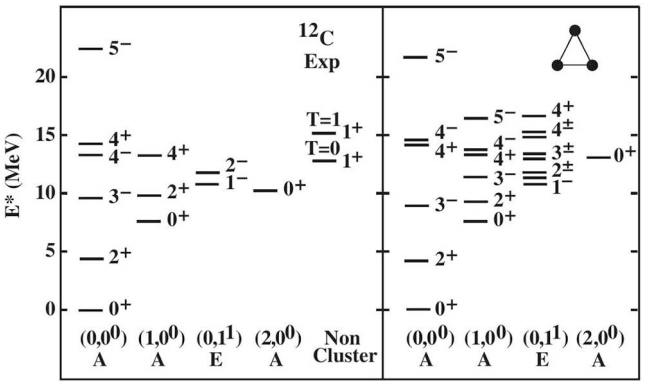

Fig. 21. The structure of ^{12}C predicted by the U(7) model [137] of a triangular spinning top with a D_{3h} symmetry compared to measured states. Note the "missing" low-spin (2^+, 3^-) states predicted by this model that can be measured with gamma-beams at the ELI-NP facility. Reprinted figure with permission from ref. [137]. Copyright (2014) by the American Physical Society.

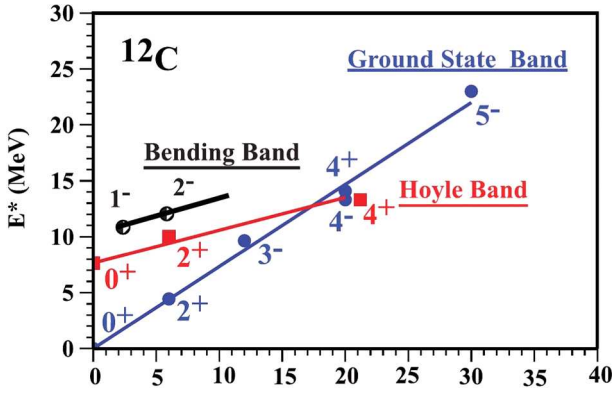

Fig. 22. All thus far observed $T = 0$ states in ^{12}C grouped into the $(K = 0, 3)$ ground state band and Hoyle state band and the $(K = 1, 2)$ bending mode band shown in fig. 21. Note the predicted (but "missing") 3^- and 4^- states in the Hoyle band and the predicted (but "missing") degenerate 2^+ state in the bending mode band shown in fig. 21. We propose to search for such 2^+ states in ^{12}C. Reprinted figure with permission from ref. [137]. Copyright (2014) by the American Physical Society.

with SSD are also considered for the ELI-NP. We emphasize that the measurements we discuss below in ^{12}C and ^{16}O are considered as typical examples of studies in nuclear structure that can be performed with our proposed detectors at the ELI-NP and such measurements in other light nuclei will lead to a new perspective on the clustering phenomena in light nuclei.

One of the most tantalizing models of clustering in ^{12}C and ^{16}O uses the geometrical symmetry of an equilateral triangle (D_{3h}) and a tetrahedral (T_d) to describe ^{12}C [136, 137] and ^{16}O, respectively [138]. Triangular configurations are indeed ubiquitous in physics as observed in the structure of hadrons (proton) [139,140], the H_3^+ molecule [141] and predicted for ^{12}C [136]. This U(7) model [136] predicts the existence of parity doublets as shown in fig. 21 and the most unusual rotational band sequence including the states: 0^+, 2^+, 3^-, $4^\pm$, 5^-, etc. [137] shown in fig. 22.

This unusual rotational band resembles the 0^+, 1^-, 2^+ and 3^- rotational band with enhance E1 decays observed for the $\alpha + {}^{14}$C structure in ^{18}O [142] as predicted by the U(4) model of diatomic molecules [143].

First indication of such a rotational band including the predicted (almost) degenerate 4^+ and 4^- states appears to have been observed in ^{12}C [144] including a newly discovered 5^- state [137], as shown in fig. 22. Hence it is of great importance to search for the other states predicted by this U(7) model [136,137] shown in fig. 21. Indeed the predicted 2^+ states in ^{12}C can be measured with intense gamma-ray beams as was done at the HIγS facility [131]. The discovery of the missing predicted states will allow for example to elucidate the (geometrical) structure of the Hoyle state that is predicted by this U(7) model to be the first excitation vibrational breathing mode of the three alpha-particles arranged in an equilateral triangular configuration.

The high-lying states of ^{12}C and ^{16}O decay primarily by the emission of three and four alpha-particles, respectively. Hence their study was best measured by large area silicon strip detectors utilizing Dalitz plots [133–135] or O-TPC [132,131]. As was demonstrated in the measurement with the O-TPC [131] broad overlapping and interfering resonances can be studied by measuring complete angular distributions and employing a phase shift analysis. We intend to use the large area SSD and the e-TPC detectors proposed for ELI-NP to measure the three and four alpha decay of high-lying states in ^{12}C and ^{16}O, respectively, following the photo-nuclear reaction with intense gamma beams from the ELI-NP facility. Such measurements of $^{12}\mathrm{C}(\gamma, 3\alpha)$ and $^{16}\mathrm{O}(\gamma, 4\alpha)$ will provide a detailed description of the clustering phenomena in these nuclei and in particular we propose to search for the predicted ("missing") 2^+ state(s) shown in fig. 21 as was previously done in the HIγS facility [131] with the $^{12}\mathrm{C}(\gamma, 3\alpha)$ reaction.

5.2 Gamma-charged particle reactions relevant to nuclear astrophysics

The SSD and the e-TPC detectors that we propose to employ at the ELI-NP facility will be mostly used to perform accurate measurements of (very small) cross-sections of nuclear reactions of the hydrogen and helium burning processes and hence the astrophysical S-factors (as defined in [145]) that are essential for stellar evolution theory. Most importantly, we plan to measure the cross-section of the $^{16}\mathrm{O}(\gamma, \alpha)^{12}\mathrm{C}$ reaction, the time reverse of the $^{12}\mathrm{C}(\alpha, \gamma)^{16}\mathrm{O}$ reaction relevant for stellar helium burning. Indeed the production of ^{12}C via the Hoyle state in the "three alpha reaction" and of ^{16}O in the $^{12}\mathrm{C}(\alpha, \gamma)^{16}\mathrm{O}$ reaction, represent one of the first and still perhaps the most vivid examples of the anthropic principle [145]. We refer the reader to [145] for a thorough review of stellar evolution theory and the definition of the nomenclatures used in this field.

Measuring capture reactions by means of the inverse photodisintegration reaction, besides being inherently low-background measurements, have the advantage of having a different systematic uncertainty than those of characteristic charged-particle–induced reactions measured at low energies of astrophysical interest. Systematic issues for example involving the target and its deterioration, (effective) beam energy definition, etc., lead to different systematic errors and thus may allow us to resolve conflicting data.

5.2.1 The $^{16}\mathrm{O}(\gamma, \alpha)^{12}\mathrm{C}$ reaction

After hydrogen is exhausted in the stellar core, stars leave the main sequence and undergo subsequent nuclear core burning stages involving heavier nuclear species, namely, helium, carbon, neon, oxygen and silicon burning, provided that stellar masses are large enough ($M > 8M_\odot$). The outcome of helium burning is the formation of the two elements: carbon and oxygen [145]. The ratio of carbon-to-oxygen (C/O) at the end of helium burning has been identified three decades ago as one of the key open questions in nuclear astrophysics [145] and it remains so today. To solve this problem one must determine the p-wave [SE1(300)] and d-wave [SE2(300)] cross-section S-factors, defined in [145], of the $^{12}\mathrm{C}(\alpha, \gamma)^{16}\mathrm{O}$ reaction at the Gamow peak (300 keV) with an accuracy of approximately 10% or better [145].

The importance of the C/O ratio for the evolution of massive stars ($M > 8M_\odot$) that evolve to core collapse (Type II) supernova has been discussed extensively [146] but more recently it was shown that the C/O ratio is also important for understanding the ^{56}Ni mass fraction produced by lower-mass stars ($M \sim 1.4M_\odot$) that evolve into Type Ia supernova (SNeIa) [147]. Thus the C/O ratio is also important for understanding the light curve of SNeIa. Such SNeIa are used as cosmological "standard candles" with which the accelerated expansion of the universe and dark energy were recently discovered [148].

Several new measurements of the $^{12}\mathrm{C}(\alpha, \gamma)^{16}\mathrm{O}$ reaction using gamma-ray detectors have been reported [149–153] with center of mass energies in the vicinity of 1.0 MeV. However, the astrophysical S-factors were determined with very low accuracies (±40%–80%) and most importantly one cannot rule out a low value (~ 10 keV b) of the extrapolated E1 S-factor [154,155]. The new data also point out to a significant ambiguity in the value of the extrapolated E2 S-factor [156]. These new experiments used some of the highest-intensity alpha-particle beams (100–500 μA) with impressive luminosities of $10^{33}\,\mathrm{cm}^{-2}\,\mathrm{s}^{-1}$ and $10^{31}\,\mathrm{cm}^{-2}\,\mathrm{s}^{-1}$, and 4π arrays of HPGe and BaF_2 detectors, that provided large counting statistics. Yet the accuracies of the measured S-factors were limited by the quality of the measured angular distributions needed to separate the E1 and E2 components.

A major disadvantage of measuring gamma-rays is the large background from neutrons emitted from the $^{13}\mathrm{C}(\alpha, \mathrm{n})$ reaction, room background gamma-rays, cosmic rays and cosmic rays induced background and Compton scattering background. Such backgrounds were not observed in the HIγS measurements of the $^{16}\mathrm{O}(\gamma, \alpha)$ reaction [132,131] and are not expected in our proposed exper-

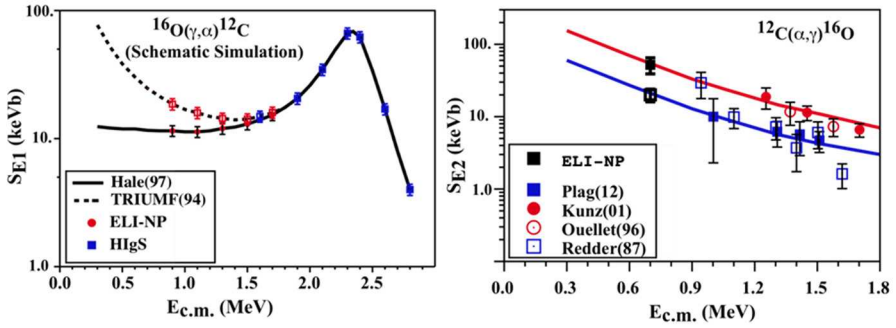

Fig. 23. The measured E2 astrophysical cross-section factors of the $^{12}C(\alpha,\gamma)$ reaction (Reprinted figure with permission from ref. [156]. Copyright (2013) by the American Physical Society) and simulated E1 astrophysical cross-section factors with gamma-beams (Reprinted from ref. [158], Copyright (2014), with permission from Elsevier).

iments utilizing gaseous TPC with the gamma-ray beams of the ELI-NP facility. In addition we will measure with the e-TPC detector detailed angular distributions, thus obtaining accurate values of the E2/E1 ratio. We however note that the proposed experiment can only measure direct-capture to the ground state. The small (less than 5%) contribution of cascade gamma-rays [157] from the $^{12}C(\alpha,\gamma)^{16}O$ reaction will not be measured in this experiment utilizing gamma-ray beams.

The principle of detailed balance allows the determination of the cross-section of an (α,γ) process from the measurement of the time inverse (γ,α) reaction with gamma-ray beams. Since both the electromagnetic and nuclear interactions are time reversal symmetric the cross-sections are related to each other in terms of the spin factors (ω) and De Broglie wavelengths by

$$\omega_A \frac{\sigma_A(X,\gamma)}{\lambda_\alpha^2} = \omega_B \frac{\sigma_B(\gamma,X)}{\lambda_\beta^2}\,. \tag{9}$$

One of the advantages of measuring the photodissociation of ^{16}O is a (50–100) gain in cross-section due to detailed balance. Such an experiment requires a gamma-ray beam of energies 10 MeV and less (approaching 8 MeV) since the Q value of the $^{12}C(\alpha,\gamma)^{16}O$ reaction is 7.162 MeV. For example a measurement of an angular distribution (2,000 counts) with the gas e-TPC detector proposed for ELI-NP, at $E_\gamma = 8.26$ MeV ($E_{c.m.} = 1.1$ MeV) with beam intensity of $10^9\,s^{-1}$ (on target) will require 21 days of beam time. Such a measurement with the gas TPC will be a continuation of the measurement with O-TPC carried out at the HIγS facility of TUNL as shown in fig. 23 [132,131].

We emphasize that the proposed measurements of the $^{16}O(\gamma,\alpha)$ photo-dissociation reaction with the gas e-TPC detector are a continuation of the studies performed at the HIγS facility [132,159,131]. As such the background and count rate estimates are well known and rely on measured values. The ELI-NP facility will provide superior gamma-beams with good energy resolution ($\sim 0.5\%$) and higher intensity ($10^9\,s^{-1}$) on target.

5.2.2 The $^{24}Mg(\gamma,\alpha)$ reaction

Silicon burning sets the chemical composition, and hence the neutron excess, of the star right before the core collapse and the subsequent supernova explosion. This demonstrates the importance of silicon burning in the understanding of core-collapse supernovae [160–162].

When ^{16}O is depleted at the conclusion of core oxygen burning, the most abundant nuclei are ^{28}Si and ^{32}S. The stellar core contracts and the temperature increases, reaching values as large as $T = 2.8$–4.1 GK, depending on the stellar mass. Fusion reactions such as $^{28}Si + {}^{28}Si$ or $^{28}Si + {}^{32}S$ are too unlikely to occur owing to the Coulomb barrier between interacting nuclei, even at such high temperatures [163]. Instead, nucleosynthesis takes place through photodisintegration of less bound nuclei and radiative captures of the dissociated light particles (protons, neutrons, and α-particles) to create gradually heavier and more tightly bound nuclei [164]. In detail, since α-particle captures on ^{20}Ne are less likely to occur than the competing (γ,α) reactions, the $^{24}Mg(\gamma,\alpha)^{20}Ne$ reaction governs the downward flow from ^{24}Mg to ^{4}He. It means that the effective rate of ^{28}Si destruction is established by the photodisintegration of ^{24}Mg, making its reaction rate critically important to stellar models of silicon burning [162].

The $^{24}Mg(\gamma,\alpha)^{20}Ne$ reaction rate has been calculated from the $^{20}Ne(\gamma,\alpha)^{24}Mg$ rate. Near $T \approx 3.6$ GK, the $^{20}Ne(\alpha,\gamma)^{24}Mg$ reaction rate may be subject to systematic errors of the order of a factor of ≈ 2, as can be seen from the different results reported by [165,166] and [167]. This is connected to the presence of a large number of resonances affecting the reaction cross-section.

A direct ^{24}Mg photodissociation measurement using gamma beams of energies 10.4–12 MeV will allow us to determine a much more accurate cross-section to be used in nuclear reaction network calculations to improve the knowledge of the pre-supernova chemical composition. Performing Hauser-Feshbach calculations of the $^{20}Ne(\alpha,\gamma)^{24}Mg$ cross-section [168] a value of approximately 0.5 mb is obtained for the reverse process in this gamma-ray energy region, corresponding to about 3×10^4

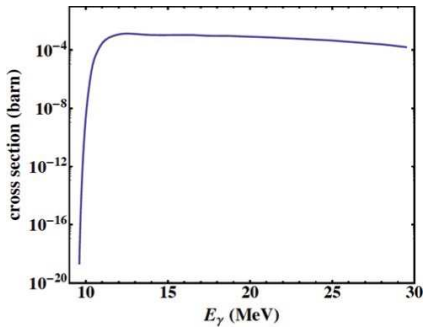

Fig. 24. Cross-section of the $^{24}\mathrm{Mg}(\gamma,\alpha)^{20}\mathrm{Ne}$ reaction estimated by applying the detailed balance principle to the $^{20}\mathrm{Ne}(\alpha,\gamma)^{24}\mathrm{Mg}$ cross-section, calculated using the Hauser-Feshbach approach [168].

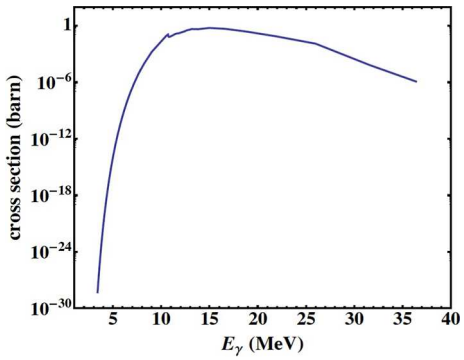

Fig. 25. Cross-section of the $^{96}\mathrm{Ru}(\gamma,\alpha)^{92}\mathrm{Mo}$ reaction estimated by applying the detailed balance principle to the $^{92}\mathrm{Mo}(\alpha,\gamma)^{96}\mathrm{Ru}$ cross-section, calculated using the Hauser-Feshbach approach [168].

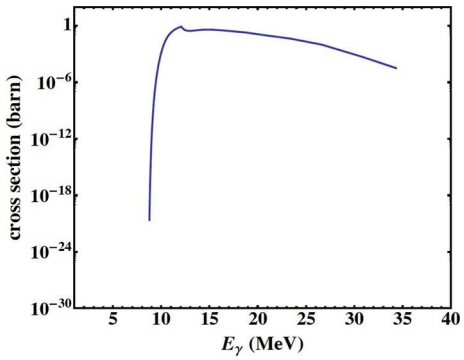

Fig. 26. Cross-section of the $^{74}\mathrm{Se}(\gamma,\mathrm{p})^{73}\mathrm{As}$ reaction estimated by applying the detailed balance principle to the $^{73}\mathrm{As}(\mathrm{p},\gamma)^{74}\mathrm{Se}$ cross-section, calculated using the Hauser-Feshbach approach [168].

reaction events per day, using a conservative beam intensity of $5\times10^3\gamma/\mathrm{s/eV}$. The estimated $^{24}\mathrm{Mg}(\gamma,\alpha)^{20}\mathrm{Ne}$ cross-section is displayed in fig. 24.

Photodissociation reactions are in principle easier to study as the phase space factor enhances the (γ,α) cross-section with respect to the inverse process, provided that a high-quality gamma beam is available, such as the one delivered by the ELI-NP facility. It is worth noting that alpha particles are emitted with energies of about 2 MeV, making it necessary to use a low-threshold detector.

It is important to note that particle identification and background suppression, due to reactions on impurities and especially on the target backing, can be effectively achieved if the reaction kinematics is recorded, since the $^{24}\mathrm{Mg}(\gamma,\alpha)^{20}\mathrm{Ne}$ reaction is a binary process. This is possible because at a known fixed angle alpha particles are emitted with a well-determined energy, making it possible to gate on this region to determine the differential cross-section. For instance, $^{12}\mathrm{C}$ photodissociation leads to three alpha-particles in the exit channel ($Q=-7.27\,\mathrm{MeV}$), with a reaction kinematics totally different from the one of a two-body process. Further simulations are necessary to verify that three-alpha kinematics is smooth, thus easily separable from the $^{24}\mathrm{Mg}(\gamma,\alpha)^{20}\mathrm{Ne}$ one. In any case, silicon detectors allow for particle identification through pulse-shape analysis and TOF to reject (γ,p) events.

5.2.3 Reactions relevant to the *p*-process

A common feature of *p*-process calculations is the underproduction of species such as $^{92}\mathrm{Mo}$, $^{94}\mathrm{Mo}$, $^{113}\mathrm{In}$ and $^{115}\mathrm{Sn}$, pointing at an unsolved problem of current *p*-process computations [162]. Nuclei such as $^{74}\mathrm{Se}$, $^{78}\mathrm{Kr}$, $^{84}\mathrm{Sr}$, $^{92}\mathrm{Mo}$, and $^{96}\mathrm{Ru}$ show a very strong dependence on the (γ,p) cross-section, making it necessary a more thoroughly investigation of the corresponding photodissociation reactions [169]. Another critical process is the $^{96}\mathrm{Ru}(\gamma,\alpha)^{92}\mathrm{Mo}$ reaction, whose cross-section changes the final abundance of $^{96}\mathrm{Ru}$ by a factor of 2 if the reaction rate is changed by a factor of 3, which is a very realistic posibility taking into account the uncertainties in the nuclear model calculation [169]. It is worth noting that most the reactions above involve nuclear species that are unavailable in gaseous form, making the use of a silicon strip detector very useful for the investigation of the corresponding photodissociation reactions. An exception is $^{78}\mathrm{Kr}$, which is a gas at NTP.

Hauser-Feshbach calculations of the $^{92}\mathrm{Mo}(\alpha,\gamma)^{96}\mathrm{Ru}$ cross-section [168] yield a value of approximately 18 mb for the reverse process at a gamma-ray energy of 9.3 MeV, that is, the energy at which such photodissociation reaction is most effective in astrophysical environments (type II supernova). Using this cross-section would yield about 6.6×10^5 reaction events per day, using the conservative beam intensity of $5\times10^3\gamma/\mathrm{s/eV}$ onto a $100\,\mu\mathrm{g/cm}^2$ target. The estimated $^{96}\mathrm{Ru}(\gamma,\alpha)^{92}\mathrm{Mo}$ cross-section is displayed in fig. 25.

Using the same Hauser-Feshbach approach for the $^{74}\mathrm{Se}(\gamma,p)^{73}\mathrm{As}$ cross-section [168], a value of approximately 250 mb is obtained by applying the detailed balance principle to the reverse process for a gamma energy of 11.1 MeV. This is the energy at which such photodissociation reaction is most effective in type II supernovae. Such cross-section would yield about 1.2×10^7 reaction events per day, using the conservative beam intensity of $5\times10^3\gamma/\mathrm{s/eV}$ onto a $100\,\mu\mathrm{g/cm}^2$ target. The estimated $^{74}\mathrm{Se}(\gamma,p)^{73}\mathrm{As}$ cross-section is displayed in fig. 26.

6 Photofission studies

Photofission measurements enable selective investigation of extremely deformed nuclear states in the light actinides and can be utilized to better understand the landscape of the multiple-humped potential energy surface (PES) in these nuclei [170,171]. The selectivity of these measurements originates from the well-defined amount of angular momentum transferred during the photoabsorption process. High-resolution studies can be performed on the mass, atomic number, and kinetic energy distributions of the fission fragments following the decay of states in the first, second and third minima of the PES in the region of the light actinides. We aim at investigating the heavy clusterization and the predicted cold valleys of the fission potential. Moreover, a special focus on the fission dynamics and clusterization effects in super- (SD) and hyper-deformed (HD) compound states will be addressed. On the other hand, by mapping the PES of the actinides the harmonicity of the potential barrier can be examined and the parameters of the fission barrier can be extracted. Fission barrier parameters are crucial inputs for cross-section calculations in the thorium-uranium fuel cycle of 4th-generation nuclear power plants. The selectivity of the photofission measurements allows high-resolution investigation of fission resonances in photofission in the 2nd and 3rd minimum of the fission barrier of the light actinides. Detailed study of SD and HD states via transmission resonance spectroscopy is relevant also for a much cleaner energy production by an efficient transmutation of the long-living, most hazardous radioactive component of the nuclear waste, and by controlling the fission process with using entrance channels via HD states. Another topic which can be addressed is the search for exotic fission modes like true ternary fission, collinear cluster tripartition (CCT) and "lead radioactivity". It will be very interesting to study the nuclear fission accompanied by light charge particle emission, to measure the light particle decay of excited states and to search for the predicted enhanced α decay of HD states of the light actinides.

6.1 Previous results obtained by photofission

Until now, sub-barrier photofission experiments have been performed only with bremsstrahlung photons and have determined integrated fission yields [170,171]. In these experiments, the fission cross-section was convolved with the spectral intensity of the photon beam, resulting in a typical effective γ-ray bandwidth of only $\Delta E/E \approx 6 \times 10^{-2}$. However, a plateau was observed in the fission cross-section, referred to as the "isomeric shelf", presumably as a result of the competition between prompt and delayed photofission [3, 4]. Due to the lack of high-resolution photofission studies in the corresponding energy region ($E \approx$ 4–5 MeV), no experimental information exists to confirm this concept. ELI-NP offers an opportunity to overcome previous limitations. The capabilities of this next-generation γ source allow one to aim at identification of sub-barrier transmission resonances in the fission decay channel with integrated cross-sections down to $\Gamma\sigma \approx 0.1$ eV b. The narrow energy bandwidth will also allow for a significant reduction of the presently dominant background from non-resonant processes. Thus, ELI-NP is expected to allow preferential population and identification of vibrational resonances in the photofission cross-section and ultimately to enable observation of the fine structure of the isomeric shelf.

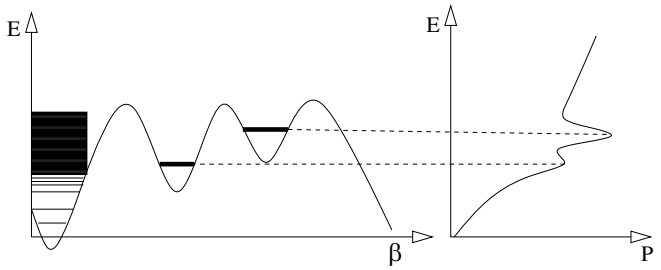

Fig. 27. Schematic illustration of the resonant tunneling process through the fission potential.

6.2 Excited states related to the fission barrier

It has been known for a long time that the fission barrier can be studied by measuring the fission probability as a function of the excitation energy [170,171]. If the energy is well below the fission barrier, then one is dealing with a classical tunneling process via the barrier. The fission probability increases exponentially with the energy. In the WKB approximation, the probability of tunneling through the barrier can be calculated by assuming a parabolic fission barrier with two parameters: the height and the curvature. The experimentally determined fission probabilities can then be compared to the results obtained with the WKB expression and the height and the curvature of the barrier can be determined.

However, the experimental fission probability is usually more complicated by the so-called fission or transmission resonances. The presence of the transitional states introduced by Bohr [172] above the top of the fission barrier, are expected to give a resonant structure in the fission probability. Several experiments observed such transition states, and gave their spectra [173].

If the fission barrier has a more complicated structure, than we may expect resonances also below the fission barrier, which can be caused by the resonant tunneling process via the excited states associated to the different minima of the fission potential as illustrated in fig. 27 [5].

6.3 Theoretical predictions and experimental data available for the fission barrier

In the actinide region, the appearance of a deep, local superdeformed second minimum in the potential energy surface of the nucleus at large quadrupole deformations was already observed experimentally and described within the macroscopic-microscopic theoretical framework long

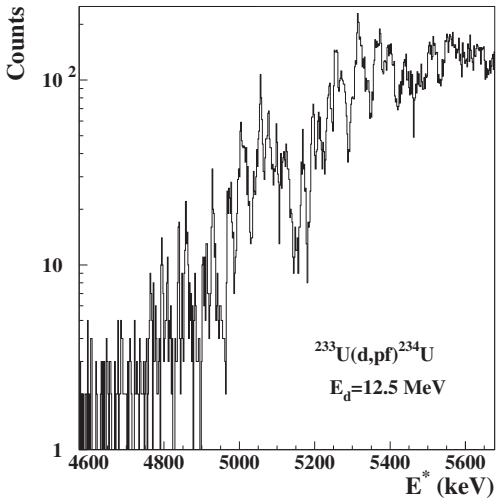

Fig. 28. Proton spectrum measured in coincidence with the fission fragments [179].

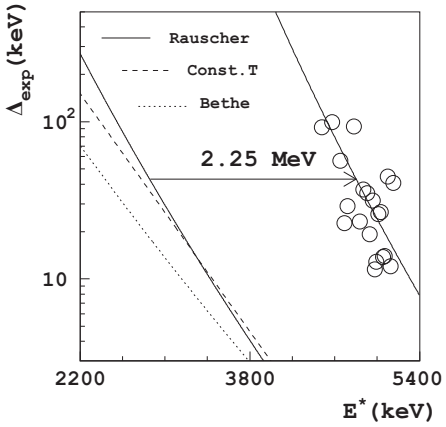

Fig. 29. Distance of the $J^\pi = 0^+$ levels in ^{240}Pu [182] as a function of the excitation energy. The solid line on the left side of the figure corresponds to the level distances in the first minimum calculated in the framework of the back-shifted Fermi gas model in a parameterization by Rauscher and co-workers [183].

time ago [174]. Later, unexplained structures in the fission cross-sections of the light actinides pointed to extend the existing picture with the triple-humped fission barrier concept with a shallow 3rd minimum in the PES at extremely large quadrupole and large octupole deformations [175–177]. Recently, it was found experimentally in several measurements on the Uranium isotopes [178–181, 5] that the 3rd minimum is in fact as deep as the 2nd minimum.

Theoretical considerations also predicted that the HD minimum in a cluster description consists of a spherical ^{132}Sn-like component with magic neutron and proton numbers of $N = 82$ and $Z = 50$, respectively, complemented by an attached elongated second cluster of nucleons. Since the fission mass distribution is distinctly determined by the configuration at the scission point, and the 3rd minimum is very close to the scission configuration, we expect that the mass distributions originating from the 3rd minimum exhibit a much more pronounced asymmetric mass distribution. However, such a dramatic effect of the shell structure has not been observed so far.

The richness of the resonances is illustrated in fig. 28 for ^{234}U. The ^{233}U(d, pf)^{234}U reaction has been studied with a very high energy resolution of $\approx 3\,\mathrm{keV}$ ($\Delta E/E = 0.1\%$). The observed fission resonances were described as members of rotational bands with rotational parameters characteristic to the hyperdeformed nuclear shape ($\hbar^2/2\theta = 2.1 \pm 0.2\,\mathrm{keV}$) [179]. Information on the K values of the bands has been obtained from fission fragment angular distribution measurements. The level density of the most strongly excited $J = 3$ states has been compared to the prediction of the back-shifted Fermi-gas formula and the energy of the ground state in the third minimum has been estimated to be $E_{\mathrm{III}} = 3.1 \pm 0.4\,\mathrm{MeV}$ [179].

In order to illustrate the reliability of the method for determining the depth of the third minimum, in fig. 29 the experimentally observed 0^+ level distances in the transmission resonance groups of ^{240}Pu [182] (open circles) are compared to calculations of the level density in the first minimum according to different models.

The solid line on the left side of the figure corresponds to the level distances in the first minimum calculated in the framework of the back-shifted Fermi gas model in the parameterization by Rauscher and co-workers [183]. In order to reproduce the experimentally observed 0^+ level distances, this curve was shifted by 2.25 MeV, corresponding to the ground-state energy in the second minimum of ^{240}Pu. For comparison, also shown are the level distances in the first minimum calculated with the Bethe formula and within the "constant temperature" formalism in a parameterization by von Egidy *et al.* [184]. The value of $E_{\mathrm{II}} = (2.25 \pm 0.20)\,\mathrm{MeV}$ —extracted for the excitation energy of the ground state in the second minimum of ^{240}Pu— is in good agreement with the fission isomer energy obtained from the well-known method of extrapolated excitation functions of various experiments ([171] and references therein). Thus, having proven the reliability of this method, an excellent tool has been obtained to address the question of the depth of the hyperdeformed third minimum of the potential surface.

6.3.1 The fission-barrier landscape

All presently available information on fission barrier parameters in the actinide mass region is shown in fig. 30 [5].

Solid blue and red squares display the barrier heights for ^{236}U as well as an estimate for the inner barrier in ^{232}Th. The solid lines represent the trends visible in the data. While previous publications favored the increase of E_{A} with decreasing Z [185] as shown by the dashed blue line, the more recent experimental information, in agreement with earlier calculations, indicates a lowering of E_{A} as illustrated by the solid blue line below Pu. This discrepancy is explained by the fact that at the time of Bjornholm and Lynn [185] the existence of a deep third minimum was

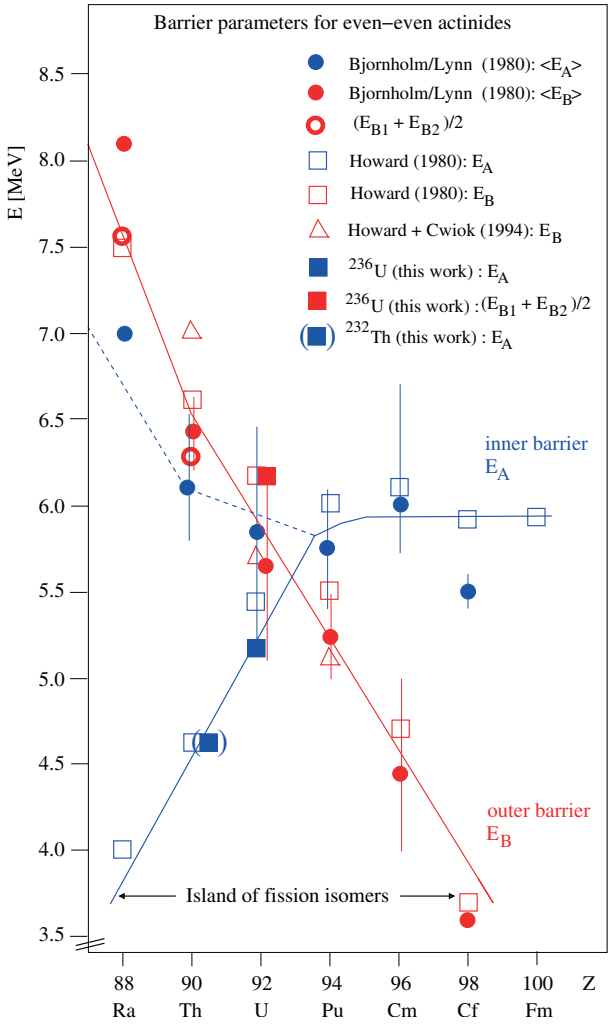

Fig. 30. Fission-barrier parameters of actinide isotopes. Red symbols indicate the outermost fission barrier E_B, while blue symbols stand for the innermost barrier E_A. The experimental data points from the compilation by Bjornholm and Lynn [185] are given by the full circles, indicating the centroid of the barrier parameters for a given Z with the error bars denoting the respective range of barrier heights. Open circles indicate the average value of the two outer barriers for the triple-humped barrier in Ra and Th. Open squares show calculated barrier heights taken from Howard and Möller [186], while open triangles contain, in addition to the calculations by Howard, information on the depth of the third potential well according to Cwiok *et al.* [187].

not known. In the paper of Britt *et al.* [188], unease about the obvious discrepancy to the theoretical expectations for E_A in ^{228}Th is explicitly expressed; however, the interpretation of the experimental data was misguided by the assumption of a double-humped fission barrier. In view of the present knowledge, the theoretical trend of a drastic lowering of the inner barrier height with decreasing Z is clearly confirmed. Figure 30 impressively locates the occurrence of the island of fission isomers in the mass region of the light actinides. With the continuous decrease of the outer barrier height E_B with increasing Z, the corresponding half-life of isomeric fission drops below the picosecond region for $Z > 98$. Quite similarly, the decrease of the inner barrier height E_A with decreasing Z results in subpicosecond half-lives for the γ back-decay in the region of $Z < 88$ thus marks the lower limit for the island of shape isomers.

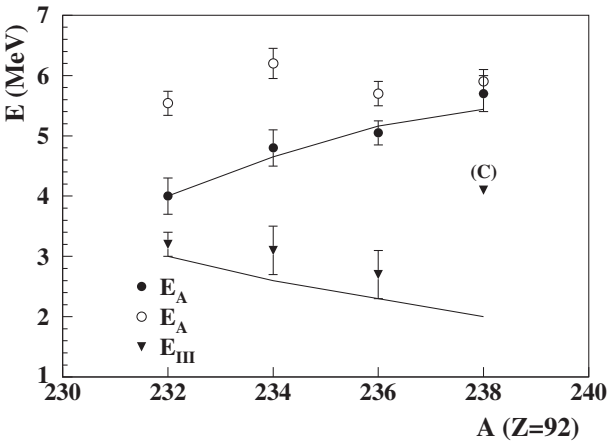

Fig. 31. The heights of the innermost barrier (EA) and the depths of the third well (EIII) for even-even uranium isotopes. The experimental data for ^{232}U, ^{234}U, ^{236}U, and ^{238}U indicated by full circles and full triangles were taken from Csige *et al.* [181]; Krasznahorkay *et al.* [179]; Csatlós *et al.* [180]; Krasznahorkay [189]; Royer and Bonilla [190], while the experimental data represented by open circles were taken from Back *et al.* [191]. Data points marked by (C) are results of calculation taken from Royer and Bonilla [190]. The upper full curve represents theoretical results for the height of the inner barrier (Howard and Möller [186]), while the lower full curve shows the theoretical E_{III} values (Cwiok *et al.* [187]).

Figure 31 shows the experimentally determined fission-barrier parameters for U isotopes as a function of mass number. The innermost barrier heights and the depths of the third well are marked by full circles and stars, respectively.

The value for the third minimum of the fission barrier of ^{238}U results from a theoretical calculation, taken from Royer and Bonilla [190]. In fig. 31, the fission-barrier parameters (assuming double-humped fission barrier) obtained by Back *et al.* [191] are indicated by open circles. The data for the inner barrier heights E_A (full circles) reveal a clear trend within the isotopic chain. Figure 31 also shows a nice agreement between the latest experimental and theoretical results for the fission-barrier parameters supporting strongly the claim that a third minimum exists. The findings assemble into a firm evidence for the existence of a deep third minimum of the fission potential.

On the other hand, recent theoretical calculations using a macroscopic-microscopic approach do not predict the existence of a deep third minimum for the even-even uranium isotopes [192,193]. This puzzle was more recently addressed within a self-consistent theoretical model, where the conditions for the existence of HD potential minima were studied in details [194].

6.3.2 Fission barrier parameters needed in data evaluation

The multi-humped fission barrier as a function of the quadrupole deformation, can be either described numerically by microscopic predictions or parametrized as parabolas smoothly joined defined by heights and widths. Such barriers are associated to the different excited states of the nucleus representing Bohr's fission channels. For the deformations corresponding to the saddle points these states are known as transitional states. For the deformations corresponding to the first, second (if the case third) minima of the fission path they are classified as class I, II (and III) respectively. The transitional states have a discrete and continuous energy spectrum. The continuous part is described by level densities which include collective enhancement factors specific to the asymmetry of the nuclear shape at each saddle point.

The parameters which describe the fundamental barrier, the discrete transitional states, the class II (and III) states and the level densities at the saddle points represent the typical input for the fission formalism presently used in fission cross-section evaluation. Such a formalism, implemented in the EMPIRE code [195], which calculates the transmission through multiple humped barriers was developed based on the optical model for fission and WKB approximation by using a recursive method [196]. It accounts for the fission mechanisms associated to the different degrees of damping of the vibrational states accommodated by the minima of the fission path and therefore can describe fission cross-sections on extended energy ranges including the resonance structure at subbarrier energies.

Most of the theoretical predictions in literature and systematics as those presented in the previous subsection provide the maxima and minima of the fission path [197], and sometimes the associated level densities [198]. They are important because they set trends, but the accuracy of their predictions is not yet good enough for evaluation. Therefore the experimental information remain crucial.

A condition to extract barrier parameters from the analysis of experimental fission cross-sections or fission probabilities is to populate the fissioning nucleus in states with excitation energies lower than barrier. This happens in neutron induced fission on fertile actinides, in direct transfer reactions such as (d,pf) and in photofission.

The advantages of the neutron induced fission are the wealth of experimental data and the capability of an accurate modelling. In this case, the barrier parameters deduced by analyzing the slope and the threshold of the cross-section, the position and the shape of the resonances combined with information from other sources such as the lifetime of the isomeric state or the asymmetry of the nuclear shape at saddles can be tested by comparing the model calculations with the experimental data. The biggest disadvantage is that fissile nuclei are populated in states with excitation energies higher than the fundamental barrier and extracting inependent information on different parameter types from the analysis of the experimental fission cross-section is almost impossible. The capability of the optical model for fission to describe the fission cross-section of light actinides was tested in [199] for ^{232}Th and ^{231}Pa. The spectacular resonance structure of these nuclei with triple-humped fission barrier was nicely reproduced using shallow third minima.

As proven in the previous Section, the experimental study of transfer reactions followed by fission such as (d,pf) represents a source of very valuable information. The only disadvantage is related to the different mechanisms (break-up, stripping, compound nucleus) contributing to (d,p) reaction which makes its modelling rather uncertain.

Photo-fission in turn, does not seem to have disadvantages, except the present scarcity of data. By photo-absorption actinide nuclei can be populated in excited states with energies well below the fission threshold. Usually, the photo-fission cross-section becomes measurable for incident photon energies above 3–4 MeV, meaning excitation energies lower than the top of the ground-state barrier with 1–3 MeV. This allows to explore the fission barrier and the transmission resonances. On the other hand, due to the predominantly E1 interaction, a high spin and parity selectivity occurs reducing the number of fission channels. All these make the interpretation of experimentally measured cross-sections significantly easier for all nuclei, irrespective on their even-odd character. The obtained information is cleaner and richer and equally important for nuclear structure and nuclear reactions, for basic and applied physics.

Ideally, a reliable, model-independent systematics for the parameters entering the description of the fission barrier should be created by corroborating all the available information provided by photo-fission, neutron-induced fission, direct transfer reactions followed by fission and global microscopic predictions. This is based on the assumption that the fission parameters are related mainly to the structure properties of the nucleus, therefore they should be independent of the way the nucleus was populated. More reliable and consistent constraints can be impose by using chains of isotopes and ensuring that for a given nucleus, the same set of parameters describes, within uncertainty limits, the first, second or third chance fission. This cross-checking procedure is expected to conduct towards an improved set of fission parameters, a validation of the reaction models and parameters and more accurate cross-section evaluations. It would provide also information about the fission parameter uncertainties, difficult to estimate otherwise and extremely important for covariance calculations.

In fig. 32 is presented the first chance of the neutron-induced fission cross-section ^{234}U(n, f) calculated with the latest fission formalism implemented in EMPIRE code (not published yet) compared to experimental data from EXFOR. Figure 33 shows the first chance photofission cross-section ^{235}U(n, f) calculated with the same fission formalism, the very same triple-humped fission barrier parameters and EMPIRE's default models and parameters for the competing channels. To get the same excitation energy of the compound nucleus in both cases, we mention that the neutron separation energy in ^{235}U is approximately 5.3 MeV. Comparing these excitation function is very instructive. The fair description of the experimen-

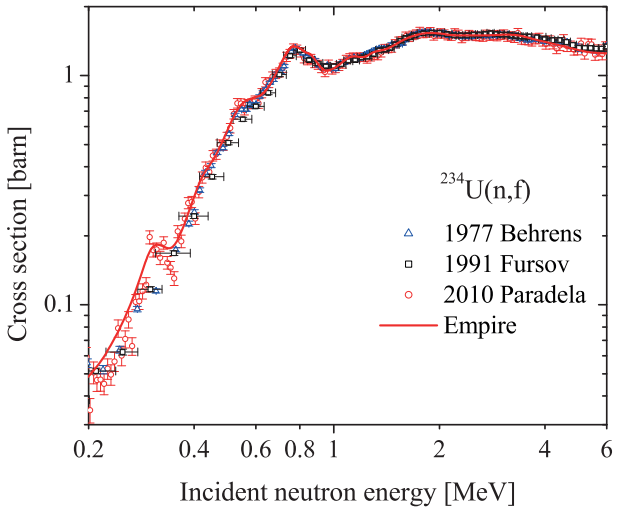

Fig. 32. Neutron-induced fission cross-section of ^{234}U. EMPIRE calculations are compared with selected experimental data retrieved from EXFOR [200].

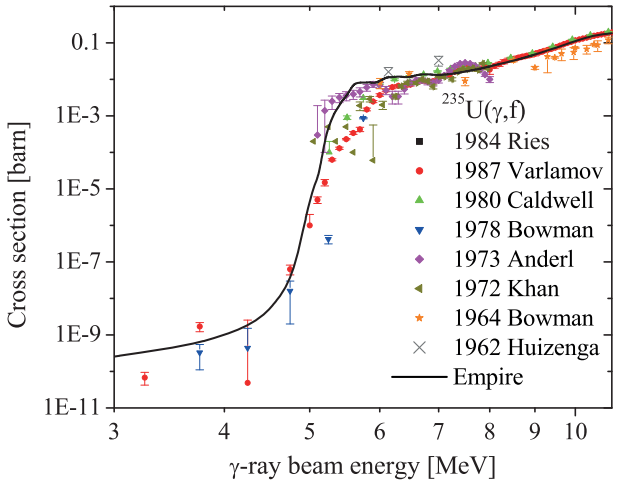

Fig. 33. Photon-induced fission cross-section of ^{235}U. EMPIRE calculations are compared with selected experimental data retrieved from EXFOR [200].

tal photofission at excitation energies higher than 8 MeV proves mainly the correctness of the humps parameters and of the level densities at the saddle points. The right energies of the resonances confirm the depth of the wells and the energies of class II and III vibrational states. The overestimation of the photofission around the threshold could indicate a wrong distribution of spin projection and parity of the transitional states. Continuing this comparison one can get information not only on fission parameters but also on the models specific to each reaction. One can notice also in fig. 34 around 7.5 MeV a hump in experimental photofission and a dip in the neutron induced cross-section which would need further investigation. This example proves the need of experimental photofission measurements as support for the evaluators to reach the tight target uncertainties for the fission data required by the sensitivity analyses for GenIII+, GenIV, Accelerator Driven Systems, Th-U fuel cycle etc.

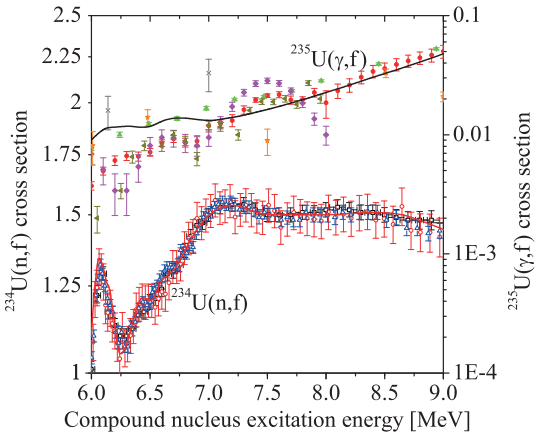

Fig. 34. Inset of figs. 32 and 33, where the neutron-induced fission cross-section of ^{234}U and the photon-induced fission cross-section of ^{235}U are represented *versus* the excitation energy of the ^{235}U compound nucleus.

6.3.3 Experimental plans at ELI-NP

Our experimental approach to investigate extremely deformed collective and single particle nuclear states of the light actinides is based on the observation of transmission resonances in the prompt fission cross-section. Observing transmission resonances as a function of the excitation energy caused by resonant tunneling through excited states in the 3rd minimum of the potential barrier, allows us to identify the excitation energies of the HD states. Moreover, the observed states can be ordered into rotational bands, with moments of inertia proving that the underlying nuclear shape of these states is indeed a HD configuration. For the identification of the rotational bands, the spin information can be obtained by measuring the angular distribution of the fission fragments. Furthermore, the PES of the actinides can be parametrized very precisely by analyzing the overall structure of the fission cross-section and by fitting it with nuclear reaction code (EMPIRE 3.1 and TALYS 1.2) calculations.

So far, transmission resonances have been studied primarily in light- particle-induced nuclear reactions. These studies do not benefit from the same selectivity found in photo-nuclear excitation and consequently they are complicated by statistical population of the states in the 2nd (and 3rd) minimum with a probability of 10^{-4}–10^{-5}. This leads to a typical isomeric fission rate from the ground-state decay of the shape isomer in the 2nd minimum of only ~ 1/sec. These measurements have also suffered from dominating prompt-fission background.

In order to test the feasibility of the experiments, the photofission cross-section of ^{238}U was measured at sub-barrier energies as a function of the γ-ray energy using a monochromatic, high-brilliance, Compton-backscattered γ-ray beam [201]. The experiment was performed at the High-Intensity γ-ray Source (HIγS) facility at beam energies between $E_\gamma = 4.7$ MeV and 6.0 MeV and with $\sim 3\%$ energy resolution. Indications of transmission resonances have been observed at γ-ray beam energies of $E_\gamma = 5.1$ MeV and 5.6 MeV with moderate amplitudes.

The triple-humped fission barrier parameters of ^{238}U have been determined by fitting EMPIRE-3.1 nuclear reaction code calculations to the experimental photofission cross-section.

6.4 Rare fission modes, ternary fission

Information about ternary fission comes from neutron-induced and spontaneous fission experiments [171]. Since ternary particles are released close to the scission point, they provide valuable information about the scission point and the fission dynamics itself.

Ternary photofission has never been studied. Compared to neutron-induced or spontaneous fission experiments, the use of polarized γ beam fixes the geometry of the process, which is an advantage for detail studies. Among the open problems related to the process are the mechanism of emission of ternary particles and the role of the deformation energy, the role of the spectroscopic factor, the formation of heavier clusters, to list a few.

Experiments at ELI-NP will provide first information about ternary photofission. The availability of brilliant γ beams will make possible detailed studies of the angular distribution of the ternary particles and provides a unique probe of the nucleus at the scission point.

6.5 Detector developments

These studies call for developments of state-of-the-art fission detectors to exploit the unprecedented properties of the high-flux, Compton backscattered γ beams having a very small, sub-millimeter beam spot size. A multi-target detector array is under development at MTA Atomki, consisting of position sensitive gas detector modules based on the state-of-the-art THGEM technology [202]. The foreseen unprecedented sub-millimeter γ beam-spot size allows to develop considerably more compact photofission detectors than those of before. Besides, the well-focused γ beam also defines a distinct fission position, so a remarkably improved angular resolution can be achieved. For the measurement of the mass and atomic number distribution of the fission fragments a highly efficient, five-folded, Frisch-gridded twin-ionization chamber [203] (used as Bragg ionization chamber [204]) is under development at MTA Atomki. The chamber will be equipped with double-sided Si strip detectors in order to measure light particle (α) emission probability from the highly deformed compound state and to detect any ternary particles from fission. An increased α decay probability would also be a conclusive evidence for the HD structure of the fissioning system. Atomic numbers will be extracted by tracking the range of the fragments using fast digitizers and advanced digital signal processing (DSP) techniques.

6.6 Simulations on photofission experiments

In order to asses the production rates of photofission fragments and the efficiencies of the various experimental setups described below, the photofission process was implemented in the Geant4.10 simulation software, deriving from its G4HadronInelasticProcess class. The photofission process, which was not available in Geant4, has been implemented as a new G4PhotoFission class [205]. The new process for gamma particles uses the existing measurements of the photofission GDR cross-sections on several actinide targets [206]. The final state of the interaction is modeled using the various measurements of photofission product distributions in the 5–20 MeV photon energy range [207–209].

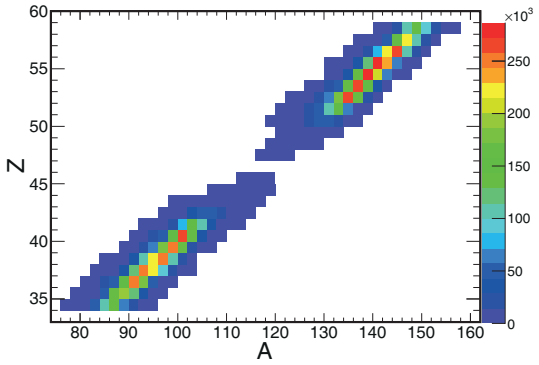

Fig. 35. Isotopic production rates from Geant4 simulations of the photofission of 800 mg ^{238}U exposed to $2.4 \cdot 10^{10}$ photons/s in the 10–18.6 MeV energy interval, corresponding to a total rate of 10^7 fissions/s.

In particular, preliminary simulations on the production rates of photofission fragments in a stack of thin ^{238}U targets were performed. The material used for the simulation is 800 mg. Figure 35 shows the (Z, A) distribution of the 10^7 ions/s which were generated.

A vast program of simulations, employing not only the Geant4 package, but also software packages like SIMION [210], SRIM [211], and other, is being developed at ELI-NP to fully characterize all the proposed experimental setups.

6.7 Separation and manipulation of neutron-rich isotopes

Different ISOL and in-fligth facilities focus on multiple aspects of studies of the structure of neutron-rich nuclei, lying away of the valley of stability. Facilities which explore photon-induced fission use intense electron beams which hit a convertor, broducing bremsstrahlung with high enough energy to excite the GDR of ^{238}U. The unique feature of ELI-NP is that the isotopes of interest can be produced in photon-induced fission using the directly the γ-ray beams with optimized energies that cover the GDR of ^{238}U. Sufficient yields of exotic nuclei are expected utilizing 10–19.5 MeV high-energy γ-ray beams.

At ELI-NP, the wide bandwidth γ-ray beam of intensity $\approx 5 \cdot 10^{10}$ γ/s will be sent on a 800 mg ^{238}U target mounted in a gas cell. Geant4 simulations of the isotope yields were performed, see fig. 35, which demonstrate that the ELI-NP IGISOL facility will be competitive to the

existing or under construction ISOL facilities for nuclear structure studies of refratory elements.

6.8 Summary on photofission experiments

The actuality of the proposed project is best represented by the previous (2010) long range plan of the Nuclear Physics European Collaboration Committee (NuPECC), in which the investigation of the fission process, in particular the low-energy collective excitations of heavy nuclei and the fine structure of the fragment mass distributions are key issues to be focused on in the following years. On the other hand, the exploration of the fission barrier landscape of the light actinides has a number of important aspects beyond fundamental nuclear physics. Development of more efficient nuclear power plants (using the Thorium fuel cycle) requires the potential energy surfaces of major and minor actinides as inputs for cross-section calculations. Nuclear fission represents a breaking-point in the astrophysical r-process, which is controlled by the fission barrier of the heavy isotopes. The precise knowledge of the PES of these nuclei is thus essential for the calculation of the heavy element abundances in the Universe, which is still one of the most compelling open problem in nuclear physics [212].

In short, in studies of fission resonances at ELI-NP one should take advantage of the resolution of the γ beam, which is about 5–7 keV in the region of interest. The γ probe excites well-defined states. There are a number of open questions related to the resonance cross-section, the resonance structure, etc., which can be addressed.

At ELI-NP an IGISOL beam line is being designed. This will provide the opportunity to study the structure of neutron-rich nuclei, isotopes of refractory elements can be extracted efficiently with the IGISOL method and, after mass and charge separation, sent to different measurement stations. Isotopes, which are difficult or impossible to be studied at ISOL facilities which use diffusion from a hot target, lie in the Ni region, in the Zr-Mo-Rh region (light fragment) and in the rare-earth region (heavy fragment). Nuclear structure studies at ELI-NP will be focused on the isotopes in the Zr-Mo-Rh region and on the rare-earth nuclei.

Conclusions

The ELI-NP facility will provide a wealth of new data related to nuclear structure, photonuclear reactions and photofission. The experiments will benefit from the beams which will be delivered by the ELI-NP gamma beam system, which are characterized by their small diameter, high-flux, narrow bandwidth and nearly 100% polarization.

At ELI-NP, NRF experiments on few mg targets become feasible, which opens the avenues for studies of rare or even radioactive targets.

In odd-N nuclei, nearly the full strength of PDR and spin-flip M1 resonances is expected to be above the neutron emission threshold. Experimental observations of the neutron and gamma decay of there resonances will be possible at ELI-NP. These studies will be complementary to the investigation of these resonances in even-even nuclei below the neutron emission threshold using the NRF technique.

In both cases, the experiments will benefit from the quality of the beams delivered by the ELI-NP. In particular, the high energy resolution and the high degree of polarization of the beams provide the possibility tu study in detail the framgmentation of the strength and to distinguish between E1 and M1 resonances.

There are noticeable and complex disagreements between total and partial photonuclear reaction data obtained in different experiments. The main reason of the disagreements is the absence of intense beams of monoenergetic photons. Because of that the results of both BR and QMA experiments are obtained indirectly and with significant systematic uncertainties which arise from usage of complicated procedures (unfolding and/or subtraction). Additionally there are significant systematic uncertainties in partial photoneutron reaction cross-sections obtained using the method of neutron multiplicity sorting primarily in QMA experiments.

A large part of photonuclear data should be remeasured in experiments free from the shortcomings mentioned above. The outstanding parameters of very brilliant intense monoenergetic γ-beam of ELI-NP project that will be obtained by means of laser Compton backscattering on accelerated electrons would produce the principally new conditions for direct measurements of photonuclear reaction cross-sections.

Nuclear reaction studies related to nuclear astrophysics will benefit from the ELI-NP γ-ray beams. Several nuclear reactions which are of key interest for present day astrophysics, like the $^{16}\mathrm{O}(\gamma,\alpha)^{12}\mathrm{C}$ and the $^{24}\mathrm{Mg}(\gamma,\alpha)^{20}\mathrm{Ne}$ reactions, are foreseen as first day experiments at ELI-NP. A special research program will focus on studies of p-process nuclei.

In the field of photofission, the effort is towards studies of fission barrier landscape and studies of rare fission events. These experiments will profit from the intense, narrow width beams of ELI-NP.

The parameters of the ELI-NP γ-ray beam provide the possibility to construct an IGISOL beamline for production of bmeas of exotic neutron-rich nuclei by photofission. This allows to study key observables of the structure of these isotopes, sending the RIBS to different measurement stations, like a β-decay spectrometer, a mass-measurementn trap, etc.

For the preparation of the program described above, a variety of codes for computer simulations have been developed. These include simulations of the γ-ray beam parameters, as well as of different photonuclear processes. As a next step, all these processes will be implemented in the Geant4.10 simulation software. Note that for some of these, as *e.g.* photofission, this is already done. This will

provide the ELI-NP team, as well as the broader user and research community, with tools to prepare experiments and evaluate physics processes.

In summary, a rich and versatile program is being prepared for the ELI-NP facility. After commisssioning in 2018, it will begin to deliver nuclear structure information from NRF experiments, data from direct measurements of photonuclear reactions, studies of nuclear collective excitations, investigations of the fission-barrier landscape and of mass, charge and angular distributions of fission fragments, as well as spectroscopic and structure studies of neutron-rich nuclei produced in photofission.

The ELI-NP team acknowledge financial support from the Extreme Light Infrastructure Nuclear Physics(ELI-NP) Phase I, a project co-financed by the Romanian Government and the European Union through the European Regional Development Fund (425/12.12.2012, POS CCE, ID 1334 SMIS-CSNR 40741). PVC thanks the support from Vietnam National Foundation for Science and Technology Development (Nafosted) under grant number 103.04-2014.29. The authors wish to express their appreciation to Prof. Dietrich Habs for his great contribution to the entire ELI-NP project starting from early stage of proposal and for his continuous support. VD, NP and AZ acknowledge financial support from the BMBF project 05P2015. MG acknowledges support from the USDOE award No. DE-FG02-94ER40870. AK acknowledges support from The Hungarian OTKA foundation No:K106035.

References

1. The ELI-NP working groups, *The White Book of ELI Nuclear Physics Bucharest-Magurele, Romania*, `www.eli-np.ro/documents/ELI-NP-WhiteBook.pdf`.
2. N.V. Zamfir *et al.*, EPJ Web of Conference **66**, 11043 (2014).
3. D. Balabanski *et al.*, Acta Phys. Pol. B **45**, 483 (2014).
4. U. Kneissl, N. Pietralla, A. Zilges, J. Phys. G **32**, R217 (2006).
5. A. Krasznahorkay, *Handbook of Nuclear Chemistry* (Springer Verlag, 2011).
6. *NewSUBARU synchrotron radiation facility, University of Hyogo*, `http://www.lasti.u-hyogo.ac.jp/NS-en/`.
7. H. Ohgaki *et al.*, IEEE Trans. Nucl. Sci. **38**, 386 (1991).
8. *High Intensity Gamma-Ray Source (HIGS), Triangle Universities Nuclear Laboratory*, `http://www.tunl.duke.edu/facilities/`.
9. D.M. Filipescu *et al.*, Phys. Rev. C **90**, 064616 (2014).
10. H.R. Weller *et al.*, Prog. Part. Nucl. Phys. **62**, 257 (2009).
11. O. Adriani *et al.*, arXiv:1407.3669 [physics.acc-ph] (2014).
12. J. Allison *et al.*, IEEE Trans. Nucl. Sci. **53**, 270 (2006).
13. S. Agostinelli *et al.*, Nucl. Instrum. Methods A **506**, 250 (2003).
14. D. Filipescu *et al.*, AIP Conf. Proc. **1645**, 322 (2015).
15. W. Bothe, W. Gentner, Z. Phys. **106**, 236 (1937).
16. C.G. Baldwin, G.S. Klaiber, Phys. Rev. **71**, 3 (1947).
17. O. Wieland *et al.*, Phys. Rev. Lett. **97**, 012501 (2006).
18. A. Shiller, M. Thoennessen, At. Data Nucl. Data Tables **93**, 549 (2007).
19. N. Paar, D. Vretenar, E. Khan, G. Colo, Rep. Prog. Phys. **70**, 691 (2007).
20. D. Savran, T. Aumann, A. Zilges, Prog. Par. Nucl. Phys. **70**, 210 (2013).
21. S. Volz *et al.*, Nucl. Phys. A **779**, 1 (2006).
22. U. Agvaanluvsan *et al.*, Phys. Rev. Lett. **102**, 162504 (2009).
23. P. Adrich *et al.*, Phys. Rev. Lett. **95**, 132501 (2005).
24. O. Wieland *et al.*, Phys. Rev. Lett. **102**, 092502 (2009).
25. D. Savran *et al.*, Phys. Rev. Lett. **100**, 232501 (2008).
26. R. Schwengner *et al.*, Phys. Rev. C **78**, 064314 (2008).
27. R. Schwengner *et al.*, Phys. Rev. C **76**, 034321 (2007).
28. R.M. Laszewski, R. Alarcon, S.D. Hoblit, Phys. Rev. Lett. **59**, 431 (1987).
29. R.M. Laszewski, R. Alarcon, D.S. Dale, S.D. Hoblit, Phys. Rev. Lett. **61**, 1710 (1988).
30. N. Pietralla, Z. Berant, V.N. Litvinenko, S. Hartman, F.F. Mikhailov, I.V. Pinayev, G. Swift, M.W. Ahmed, J.H. Kelley, S.O. Nelson *et al.*, Phys. Rev. Lett. **88**, 012502 (2001).
31. T. Shizuma *et al.*, Phys. Rev. C **78**, 061303 (2008).
32. K. Govaert *et al.*, Phys. Rev. C **57**, 2229 (1998).
33. A.P. Tonchev *et al.*, Phys. Rev. Lett. **104**, 072501 (2010).
34. G.P.A. Berg *et al.*, Phys. Rev. C **25**, 2100 (1982).
35. N. Anantaraman *et al.*, Phys. Rev. Lett. **46**, 1318 (1981).
36. F.E. Bertrand *et al.*, Phys. Lett. B **103**, 326 (1981).
37. G.M. Crawley *et al.*, Phys. Rev. C **26**, 87 (1982).
38. S.K. Nanda *et al.*, Phys. Rev. Lett. **51**, 1526 (1983).
39. C. Djalali *et al.*, Nucl. Phys. A **388**, 1 (1982).
40. C. Iwamoto, H. Utsunomiya, A. Tamii *et al.*, Phys. Rev. Lett. **108**, 262501 (2012).
41. A. Tamii *et al.*, Phys. Rev. Lett. **107**, 062502 (2011).
42. C.D. Bowman, R.J. Baglan, B.L. Berman, T.W. Phillips, Phys. Rev. Lett. **25**, 1302 (1970).
43. H. Utsunomiya *et al.*, Phys. Rev. Lett. **100**, 162502 (2008).
44. D.M. Brink, PhD thesis, Oxford University (1955).
45. H. Utsunomiya *et al.*, Phys. Rev. C **67**, 015807 (2003).
46. H. Utsunomiya *et al.*, Phys. Rev. C **80**, 055806 (2009).
47. S. Goriely, Phys. Lett. B **436**, 10 (1998).
48. S. Goriely, E. Khan, M. Samyn, Nucl. Phys. A **739**, 331 (2004).
49. A. Avdeyenkova, S. Goriely, S. Kamerdzhiev, G. Tertychny, AIP Conf. Ser. **1090**, 149 (2009).
50. V. Derya *et al.*, J. Phys.: Conf. Ser. **366**, 012012 (2012).
51. D. Savran *et al.*, Phys. Rev. Lett. **97**, 172502 (2006).
52. F. Crespi *et al.*, Phys. Rev. Lett. **113**, 012501 (2014).
53. F. Crespi *et al.*, Phys. Rev. C **91**, 024323 (2015).
54. L. Pellegri *et al.*, Phys. Lett. B **738**, 519 (2014).
55. J. Endres *et al.*, Phys. Rev. Lett. **105**, 212503 (2010).
56. E. Litvinova, P. Ring, V. Tselyaev, Phys. Rev. C **78**, 014312 (2008).
57. V.G. Soloviev, *Theory of Atomic Nuclei: Quasiparticles and Phonons* (Institute of Physics, Bristol, 1992).
58. A. Zilges, S. Volz, M. Babilon, T. Hartmann, P. Mohr, K. Vogt, Phys. Lett. B **542**, 43 (2002).
59. U. Kneissl, H.H. Pitz, A. Zilges, Prog. Part. Nucl. Phys. **37**, 349 (1996).
60. C. Romig, J. Beller, J. Glorius, J. Isaak, J.H. Kelley, E. Kwan, N. Pietralla, V.Yu. Ponomarev, A. Sauerwein, D. Savran *et al.*, Phys. Rev. C **88**, 044331 (2013).
61. K. Govaert, W. Mondelaers, E. Jacobs, D.D. Frenne, K. Persyn, S. Pomm, M.L. Yoneama, S. Lindenstruth, K. Huber, A. Jung *et al.*, Nucl. Instrum. Methods A **337**, 265 (1994).

62. K. Sonnabend, D. Savran, J. Beller, M. Büssing, A. Constantinescu, M. Elvers, J. Endres, M. Fritzsche, J. Glorius, J. Hasper *et al.*, Nucl. Instrum. Methods Phys. Res. A **640**, 6 (2011).
63. R. Schwengner, R. Beyer, F. Dönau, E. Grosse, A. Hartmann, A. Junghans, S. Mallion, G. Rusev, K. Schilling, W. Schulze *et al.*, Nucl. Instrum. Methods A **555**, 211 (2005).
64. U. Kneissl, A. Zilges, *Landolt Börnstein Volume I/25B: Excited Nuclear States* (Springer, Heidelberg, 2012).
65. H. Ohgaki, T. Noguchi, S. Sugiyama, T. Yamazaki, T. Mikado, M. Chiwaki, K. Yamada, R. Suzuki, N. Sei, Nucl. Instrum. Methods Phys. Res. A **353**, 384 (1994).
66. H. Utsunomiya *et al.*, IEEE Trans. Nucl. Sci. **61**, 1252 (2014).
67. J. Beller *et al.*, Phys. Lett. B **741**, 128 (2015).
68. B. Löher, V. Derya, T. Aumann, J. Beller, N. Cooper, M. Duchêne, J. Endres, E. Fiori, J. Isaak, J.H. Kelley *et al.*, Nucl. Instrum. Methods A **723**, 136 (2013).
69. R.J. Baglan, C.D. Bowman, B.L. Berman, Phys. Rev. C **3**, 2475 (1971).
70. R.J. Baglan, C.D. Bowman, B.L. Berman, Phys. Rev. C **3**, 672 (1971).
71. C.D. Bowman, G.S. Sidhu, B.L. Berman, Phys. Rev. **163**, 951 (1967).
72. T. Kondo *et al.*, Phys. Rev. C **86**, 014316 (2012).
73. J.R. Beene *et al.*, Phys. Rev. C **41**, 920 (1990).
74. A.V. Varlamov, V.V. Varlamov, D.S. Rudenko *et al.*, *Atlas of Giant Dipole Resonances*, INDC(NDS) 394 (1999).
75. B. Berman, S. Fultz, Rev. Mod. Phys. **47**, 713 (1975).
76. S. Dietrich, B. Berman, At. Data Nucl. Data Tables **38**, 199 (1988).
77. V. Varlamov, B. Ishkhanov, M. Stepanov *et al.*, Bull. Rus. Acad. Sci. Phys. **67**, 1733 (2003).
78. V. Varlamov, B. Ishkhanov, D. Rudenko *et al.*, Phys. At. Nucl. **67**, 2107 (2004).
79. Y.P. Pyt'ev, *Methods for an Analysis and an Interpretation of Experiments* (MSU, Moscow, 1990).
80. B. Ishkhanov, I. Kapitonov, E. Lazutin *et al.*, Vestn. Mos. Gos. Univ. Ser. 3 Fiz. Astron. **6**, 606 (1970).
81. R. Sund, M. Baker, L. Kull *et al.*, Phys. Rev. **176**, 1366 (1968).
82. J. Woodworth, K. McNeill, J. Jury *et al.*, Phys. Rev. C **19**, 1667 (1979).
83. A. Veyssiere, H. Beil, R. Bergere *et al.*, Nucl. Phys. A **227**, 513 (1974).
84. R. Bramblett, J. Caldwell, R. Harvey *et al.*, Phys. Rev. B **133**, 869 (1964).
85. S.C. Fultz, R.L. Bramblett, J.T. Caldwell *et al.*, Phys. Rev. **127**, 1273 (1962).
86. R. Pywell, M. Thompson, B. Berman, Nucl. Instrum. Methods **178**, 149 (1980).
87. V.V. Varlamov, B.S. Ishkhanov, V.N. Orlin *et al.*, Eur. Phys. J. A **50**, 114 (2014).
88. V.V. Varlamov, B.S. Ishkhanov, INDC(CCP) 433 (2002).
89. E. Wolynec, A.R.V. Martinez, P. Gouffon *et al.*, Phys. Rev. C **29**, 1137 (1984).
90. E. Wolynec, M.N. Martins, Rev. Bras. Fis. **17**, 56 (1987).
91. V.V. Varlamov, B.S. Ishkhanov, V.N. Orlin *et al.*, Bull. Rus. Acad. Sci. **74**, 842 (2010).
92. V.V. Varlamov, B.S. Ishkhanov, V.N. Orlin *et al.*, Bull. Rus. Acad. Sci. **74**, 883 (2010).
93. V.V. Varlamov, B.S. Ishkhanov, V.N. Orlin *et al.*, Phys. At. Nucl. **75**, 1339 (2012).
94. V.V. Varlamov, V.N. Orlin, N.N. Peskov *et al.*, Bull. Rus. Acad. Sci. **77**, 388 (2013).
95. V.V. Varlamov, B.S. Ishkhanov, V.N. Orlin *et al.*, Phys. At. Nucl. **76**, 1403 (2013).
96. V.V. Varlamov, M.A. Makarov, N.N. Peskov *et al.*, Bull. Rus. Acad. Sci. Phys. **78**, 412 (2014).
97. B.S. Ishkhanov, V.N. Orlin *et al.*, Phys. Part. Nucl. **38**, 232 (2007).
98. B.S. Ishkhanov, V.N. Orlin *et al.*, Phys. At. Nucl. **71**, 493 (2008).
99. S.C. Fultz, B.L. Berman, J.T. Caldwell *et al.*, Phys. Rev. **186**, 1255 (1969).
100. P. Carlos, Nucl. Phys. A **172**, 437 (1971).
101. C.T. Angell *et al.*, Phys. Rev. C **86**, 051302 (2012).
102. H.T. Nyhus *et al.*, Phys. Rev. C **91**, 015808 (2015).
103. S.N. Beljaev *et al.*, Bull. Rus. Acad. Sci. Phys. **55**, 66 (1991).
104. *Handbook on photonuclear data for applications. Cross-sections and spectra, Final report of a co-ordinated research project 1996 - 1999, IAEA-TECDOC-1178* (2000).
105. E. Anders, N. Grevesse, Geochim. Cosmochim. Acta **53**, 197 (1989).
106. S.E. Woosley, W.M. Howard, Astrophys. J. Suppl. **36**, 285 (1978).
107. M. Rayet, M. Arnould, M. Hashimoto, N. Prantzos, K. Nomoto, Astron. Astrophys. **298**, 517 (1995).
108. T. Rauscher, A. Hefer, R.D. Hoffman, S.E. Woosley, Astrophys. J. **576**, 323 (2002).
109. M. Arnould, S. Goriely, Phys. Rep. **384**, 1 (2003).
110. H. Utsunomiya, P. Mohr, A. Zilges, M. Rayet, Nucl. Phys. A **777**, 459 (2006).
111. H. Utsunomiya, M.S. Smith, T. Kajino, M. Arnould *et al.* (Editors), AIP Conf. Proc. **561**, 159 (2001).
112. S. Goko, Utsunomiya *et al.*, Phys. Rev. Lett. **96**, 192501 (2006).
113. K. Wisshak, F. Voss, C. Arlandi *et al.*, Phys. Rev. Lett. **87**, 251102 (2001).
114. H. Utsunomiya *et al.*, Phys. Rev. C **74**, 025806 (2006).
115. F.G.A. Quarati *et al.*, Nucl. Instrum. Methods A **683**, 46 (2012).
116. A. Giaz *et al.*, Conference record of IEEE-NSS (2014).
117. R. Roth *et al.*, Phys. Rev. Lett. **107**, 072501 (2011).
118. A.C. Dreyfuss *et al.*, Phys. Lett. B **727**, 511 (2013).
119. E. Epelbaum *et al.*, Phys. Rev. Lett. **106**, 192501 (2011).
120. E. Epelbaum *et al.*, Phys. Rev. Lett. **109**, 252501 (2012).
121. M. Chernykh, H. Feldmeier, T. Neff, P. von Neumann-Cosel, A. Richter, Phys. Rev. Lett. **98**, 032501 (2007).
122. Y. Kanada-Enyo, Prog. Theor. Phys. **117**, 655 (2007).
123. M. Kamimura, Nucl. Phys. A **351**, 456 (1981).
124. Y. Funaki *et al.*, Phys. Rev. C **80**, 064326 (2009).
125. H.O.U. Fynbo, M. Freer, Physics **4**, 94 (2011).
126. H. Morinaga, Phys. Rev. **101**, 254 (1956).
127. M. Itoh *et al.*, Nucl. Phys. A **738**, 268 (2004).
128. M. Freer *et al.*, Phys. Rev. C **80**, 041303 (2009).
129. W.R. Zimmerman *et al.*, Phys. Rev. C **84**, 027304 (2011).
130. M. Freer *et al.*, Phys. Rev. C **86**, 034320 (2012).
131. W.R. Zimmerman *et al.*, Phys. Rev. Lett. **110**, 152502 (2013).
132. M. Gai *et al.*, JINST **5**, 12004 (2010).
133. M. Freer *et al.*, Phys. Rev. C **76**, 034320 (2007).
134. M. Freer *et al.*, Phys. Rev. C **83**, 034314 (2011).
135. O.S. Kirsebom *et al.*, Phys. Rev. C **81**, 064313 (2010).
136. R. Bijker, F. Iachello, Ann. Phys. (N.Y.) **298**, 334 (2002).

137. D.J. Marín-Lámbarri *et al.*, Phys. Rev. Lett. **113**, 012502 (2014).
138. R. Bijker, F. Iachello, Phys. Rev. Lett. **112**, 152501 (2014).
139. S. Capstick, N. Isgur, Phys. Rev. D **34**, 2809 (1986).
140. R. Bijker, F. Iachello, A. Leviatan, Ann. Phys. (N.Y.) **236**, 69 (1994).
141. R. Bijker, A.E.L. Dieperink, A. Leviatan, Phys. Rev. A **52**, 2786 (1995).
142. M. Gai *et al.*, Phys. Rev. Lett. **50**, 239 (1983).
143. F. Iachello, Phys. Rev. C **23**, 2778 (1981).
144. M. Gai *et al.*, *10th Latin American Symposium on Nuclear Physics and Applications (X-LASNPA), Montevideo, Uruguay* (2013).
145. W.A. Fowler, Rev. Mod. Phys. **56**, 149 (1984).
146. T.A. Weaver, S.E. Woosley, Phys. Rep. **227**, 65 (1993).
147. F.K. Thielemann *et al.*, New Astro. Rev. **48**, 605 (2004).
148. S. Perlmutter, Rev. Mod. Phys. **84**, 1127 (2012).
149. R. Kunz *et al.*, Phys. Rev. Lett. **86**, 3244 (2001).
150. J.W. Hammer, Nucl. Phys. A **752**, 514 (2005).
151. J.W. Hammer, Nucl. Phys. A **758**, 363 (2005).
152. M. Assuncao *et al.*, Phys. Rev. C **73**, 055801 (2006).
153. R. Plag *et al.*, Phys. Rev. C **86**, 015805 (2012).
154. L. Gialanella *et al.*, Eur. Phys. J. A **11**, 357 (2011).
155. G.M. Hale, Nucl. Phys. A **621**, 177c (1997).
156. M. Gai, Phys. Rev. C **88**, 062801 (2013).
157. D. Schuermann *et al.*, Phys. Lett. B **703**, 557 (2011).
158. M. Gai, Nucl. Phys. A **928**, 313 (2014).
159. C. Ugalde *et al.*, Phys. Lett. B **719**, 74 (2013).
160. D. Bodansky, D.D. Clayton, W.A. Fowler, Astrophys. J. Suppl. **148**, 299 (1968).
161. S.E. Woosley, W.D. Arnett, D.D. Clayton, Astrophys. J. Suppl. **26**, 231 (1973).
162. C. Iliadis, *Nuclear Physics of Stars* (Wiley-VCH Verlag, Weinheim, 2007).
163. A.J. Howard, H.B. Jensen, M. Rios, W.A. Fowler, B.A. Zimmerman, Astrophys. J. **188**, 131 (1974).
164. W.R. Hix, F.K. Thielemann, Astrophys. J. **460**, 869 (1996).
165. G.R. Caughlan, W.A. Fowler, At. Data Nucl. Data Tables **40**, 283 (1988).
166. C. Angulo *et al.*, Nucl. Phys. A **656**, 3 (1999).
167. T. Rauscher, F.K. Thielemann, At. Data Nucl. Data Tables **75**, 1 (2000).
168. T. Rauscher, At. Data Nucl. Data Tables **79**, 46 (2001).
169. W. Rapp *et al.*, Nucl. Phys. A **758**, 545 (2005).
170. R. Vandenbosch, J. Huizenga, *Nuclear fission* (Academic Press, New York, 1973).
171. C. Wagemans, *The nuclear fission process* (CRC Press, Boca Raton, 1991).
172. A. Bohr, *Proceedings of the Geneva conference*, Vol. **2** (1955) p. 220.
173. Y. Kikuchi, S. An, J. Nucl. Sci. Technol. **7**, 157 (1970).
174. P.G. Thirolf, D. Habs, Prog. Part. Nucl. Phys. **49**, 352 (2002).
175. J. Blons, C. Mazur, D. Paya, Phys. Rev. Lett. **35**, 1749 (1975).
176. J. Blons *et al.*, Phys. Rev. Lett. **41**, 1282 (1978).
177. J. Blons, C. Mazur, D. Paya, M. Ribrag, H. Weigmann, Nucl. Phys. A **414**, 1 (1984).
178. A. Krasznahorkay *et al.*, Phys. Rev. Lett. **80**, 2073 (1998).
179. A. Krasznahorkay *et al.*, Phys. Lett. B **461**, 15 (1999).
180. M. Csatloós *et al.*, Phys. Lett. B **615**, 175 (2005).
181. L. Csige *et al.*, Phys. Rev. C **80**, 011301 (2009).
182. M. Hunyadi *et al.*, Phys. Lett. B **505**, 27 (2001).
183. T. Rauscher, F.K. Thielemann, K.L. Kratz, Phys. Rev. C **56**, 1613 (1997).
184. T. von Egidy, H.H. Smidt, A.N. Behkami, Nucl. Phys. A **481**, 189 (1988).
185. S. Bjornholm, J.E. Lynn, Rev. Mod. Phys. **52**, 725 (1980).
186. W.M. Howard, P. Möller, At. Data Nucl. Data Tables **25**, 219 (1980).
187. S. Cwiok, W. Nazarewicz, J.X. Saladin, W. Plociennik, A. Johnson, Phys. Lett. B **322**, 304 (1994).
188. H.C. Britt, M. Bolsterli, J.R. Nix, J.L. Norton, Phys. Rev. C **7**, 801 (1973).
189. A. Krasznahorkay *et al.*, Acta. Phys. Pol. B **27**, 139 (1996).
190. G. Royer, C. Bonilla, J. Radioanal. Nucl. Chem. **272**, 237 (2007).
191. B.B. Back, O. Hansen, H.C. Britt, J.D. Garrett, Phys. Rev. C **9**, 1924 (1974).
192. M. Kowal, J. Skalski, Phys. Rev. C **85**, 061302 (2012).
193. P. Jachimowicz, M. Kowal, J. Skalski, Phys. Rev. C **87**, 044308 (2013).
194. J.D. McDonnell, W. Nazarewicz, J.A. Sheikh, Phys. Rev. C **87**, 054327 (2013).
195. M. Herman, R. Capote, B.V. Carlson, P. Oblozinsky, M. Sin, A. Trkov, H. Wienke, V. Zerkin, Nucl. Data Sheets **108**, 2655 (2007).
196. M. Sin, R. Capote, Phys. Rev. C **77**, 054601 (2008).
197. T. Ichikawa *et al.*, Phys. Rev. C **87**, 054326 (2013).
198. S. Goriely, S. Hilaire, A.J. Koning, M. Sin, R. Capote, Phys. Rev. C **79**, 024612 (2009).
199. M. Sin, R. Capote, A. Ventura, M. Herman, P. Oblozinsky, Phys. Rev. C **74**, 014608 (2006).
200. *Experimental Nuclear Reaction Data (EXFOR)*, `www-nds.iaea.org/exfor/exfor.htm`.
201. L. Csige *et al.*, Phys. Rev. C **87**, 04432 (2013).
202. C.K. Shalem *et al.*, Nucl. Instrum. Methods Phys. Res. A **558**, 468 (2006).
203. C. Budtz-Jorgensen *et al.*, Nucl. Instrum. Methods Phys. Res. A **258**, 209 (1987).
204. W. Neubert, Nucl. Instrum. Methods Phys. Res. A **237**, 535 (1985).
205. Phan Viet Cuong, PhD thesis, Université de Paris - Orsay (2010).
206. J.T. Caldwell *et al.*, Phys. Rev. C **21**, 1215 (1980).
207. C. Donzaud *et al.*, Eur. Phys. J. A **1**, 47 (1998).
208. S. Pomme *et al.*, Nucl. Phys. A **572**, 237 (1994).
209. J.T. Caldwell *et al.*, Nucl. Sci. Eng. **73**, 153 (1980).
210. *SIMION charged particle optics simulation software*, `http://simion.com/`.
211. F. Ziegler *et al.*, *The Stopping and Range of Ions in Solids* (Pergamon Press, New York, 1985).
212. S. Goriely *et al.*, Phys. Rev. Lett. **111**, 242502 (2013).